CrossMark

Measurements of the Dust Properties in $z \simeq 1$–3 Submillimeter Galaxies with ALMA

E. da Cunha[1,2,3], J. A. Hodge[4], C. M. Casey[5], H. S. B. Algera[4], M. Kaasinen[6,7], I. Smail[8], F. Walter[6],
W. N. Brandt[9,10,11], H. Dannerbauer[12,13], R. Decarli[14], B. A. Groves[1,2], K. K. Knudsen[15], A. M. Swinbank[8],
A. Weiss[16], P. van der Werf[4], and J. A. Zavala[5]

[1] International Centre for Radio Astronomy Research, University of Western Australia, 35 Stirling Hwy., Crawley, WA 6009, Australia
Elisabete.daCunha@uwa.edu.au
[2] Research School of Astronomy and Astrophysics, Australian National University, Canberra, ACT 2611, Australia
[3] ARC Centre of Excellence for All Sky Astrophysics in 3 Dimensions (ASTRO 3D), Australia
[4] Leiden Observatory, Leiden University, P.O. Box 9513, 2300 RA Leiden, The Netherlands
[5] The University of Texas at Austin, 2515 Speedway Boulevard, Stop C1400, Austin, TX 78712, USA
[6] Max-Planck Institut für Astronomie, Konigstuhl 17, D-69117 Heidelberg, Germany
[7] Universität Heidelberg, Zentrum für Astronomie, Institut für Theoretische Astrophysik, Albert-Ueberle-Strasse 2, D-69120 Heidelberg, Germany
[8] Centre for Extragalactic Astronomy, Department of Physics, Durham University, South Road, Durham, DH1 3LE, UK
[9] Department of Astronomy & Astrophysics, The Pennsylvania State University, 525 Davey Lab, University Park, PA 16802, USA
[10] Institute for Gravitation and the Cosmos, The Pennsylvania State University, University Park, PA 16802, USA
[11] Department of Physics, The Pennsylvania State University, University Park, PA 16802, USA
[12] Instituto de Astrofísica de Canarias (IAC), E-38205 La Laguna, Tenerife, Spain
[13] Universidad de La Laguna, Dpto. Astrofísica, E-38206 La Laguna, Tenerife, Spain
[14] INAF—Osservatorio di Astrofisica e Scienza dello Spazio, via Gobetti 93/3, I-40129, Bologna, Italy
[15] Department of Space, Earth and Environment, Chalmers University of Technology, Onsala Space Observatory, SE-43992 Onsala, Sweden
[16] Max-Planck-Institut für Radioastronomie, Auf dem Hügel 69, D-53121 Bonn, Germany

Abstract

We present Atacama Large Millimeter/submillimeter Array (ALMA) 2 mm continuum observations of a complete and unbiased sample of 99 870 μm selected submillimeter galaxies (SMGs) in the Extended Chandra Deep Field South (ALESS). Our observations of each SMG reach average sensitivities of 53 μJy beam^{-1}. We measure the flux densities for 70 sources, for which we obtain a typical 870 μm-to-2 mm flux ratio of 14 ± 5. We do not find a redshift dependence of this flux ratio, which would be expected if the dust emission properties of our SMGs were the same at all redshifts. By combining our ALMA measurements with existing Herschel/SPIRE observations, we construct a (biased) subset of 27 galaxies for which the cool dust emission is sufficiently well sampled to obtain precise constraints on their dust properties using simple isothermal models. Thanks to our new 2 mm observations, the dust emissivity index is well constrained and robust against different dust opacity assumptions. The median dust emissivity index of our SMGs is $\beta \simeq 1.9 \pm 0.4$, consistent with the emissivity index of dust in the Milky Way and other local and high-redshift galaxies, as well as classical dust-grain model predictions. We also find a negative correlation between the dust temperature and β, similar to low-redshift observational and theoretical studies. Our results indicate that $\beta \simeq 2$ in high-redshift dusty star-forming galaxies, implying little evolution in dust-grain properties between our SMGs and local dusty galaxy samples, and suggesting that these high-mass and high-metallicity galaxies have dust reservoirs driven by grain growth in their interstellar medium.

Unified Astronomy Thesaurus concepts: Submillimeter astronomy (1647); High-redshift galaxies (734); Interstellar medium (847)

1. Introduction

Submillimeter galaxies (SMGs) are the most dust-rich galaxies in the universe, with large ($\gtrsim 10^{12} L_{\odot}$) infrared (IR) luminosities that are powered by high star formation rates (SFR $\gtrsim 100 M_{\odot} \, \mathrm{yr}^{-1}$; e.g., Blain et al. 2002; Barger et al. 2012; Casey et al. 2014; Swinbank et al. 2014; da Cunha et al. 2015; Dudzevičiūtė et al. 2020). This combination makes SMGs ideal targets for studies of dust formation and the interplay between gas, dust, and stars (e.g., Hodge et al. 2012, 2015, 2016, 2019; Swinbank et al. 2015; Chen et al. 2017; see Hodge & da Cunha 2020 for a recent review). Although SMGs are relatively rare (e.g., Weiß et al. 2009), they contribute significantly ($\gtrsim 20\%$) to the SFR density at $z > 1$ (e.g., Chapman et al. 2005; Sargent et al. 2012; Swinbank et al. 2014; Dudzevičiūtė et al. 2020), and they are likely progenitors of the most massive galaxies in the local universe (e.g., Blain et al. 2002; Casey et al. 2014; Simpson et al. 2014).

The first SMGs were detected using SCUBA at 850 μm (Smail et al. 1997; Barger et al. 1998; Hughes et al. 1998), which remains

one of the prime wavelengths to detect these galaxies (e.g., Geach et al. 2017), thanks to a combination of available instruments, spectral window, and the negative k-correction at that wavelength. Other single-dish samples of SMGs have also been obtained at 1.1–1.3 mm using MAMBO (e.g., Eales et al. 2003; Bertoldi et al. 2007; Greve et al. 2008) and AzTEC (e.g., Aretxaga et al. 2011; Yun et al. 2012), at 1.4 mm/2 mm with the SPT (Vieira et al. 2010), and at 2 mm with GISMO (Staguhn et al. 2014; Magnelli et al. 2019). Selecting SMGs from observations at longer wavelengths is thought to favor galaxies at higher redshifts (e.g., Smolčić et al. 2012; Vieira et al. 2013; Staguhn et al. 2014; Magnelli et al. 2019; Hodge & da Cunha 2020), although it is difficult to compare the redshift distributions in an unbiased way (see, e.g., Zavala et al. 2014 for a discussion), and account for intrinsic variations of galaxy far-IR spectral energy distributions (SEDs). Nevertheless, the 2 mm band has been put forth as a potential candidate to detect high-redshift ($z > 3$) galaxies (e.g., Casey et al. 2018a, 2018b, 2019; Zavala et al. 2021). The negative

k-correction is stronger at 2 mm than at 850 μm; thus, for a fixed SED, the 2 mm band should pick up more high-redshift galaxies than at 870 μm. In addition, better atmospheric transmission and larger fields of view can be achieved at 2 mm (but corresponding poorer resolution). Such an effort is currently ongoing (see Zavala et al. 2021 for first results). To understand the relationship between the populations detected at 850 μm and at 2 mm, we require a detailed characterization of the (sub)millimeter SEDs of these sources. Multiwavelength submillimeter observations are still rare, with most observations focusing on a single wavelength. Only a handful of sources observed at 2 mm have complementary shorter-wavelength detections (Staguhn et al. 2014; Magnelli et al. 2019). Thus, a more systematic multiwavelength dust continuum investigation is warranted in order to reveal the dust properties of (sub)millimeter-detected sources.

In recent years, there has been much debate over the origin of the large dust masses of SMGs (typically $\gtrsim 10^8\,M_\odot$, i.e., a few percent of their stellar mass; e.g., Dudzevičiūtė et al. 2020). However, such measurements have mostly been performed for biased samples (that favor the dustiest sources) and until recently relied solely on single-dish observations (e.g., Rowlands et al. 2014; Dudzevičiūtė et al. 2021). The buildup of such large dust masses over timescales $\sim$0.5–2 Gyr is extremely difficult to explain with models of dust production and growth relying solely on stellar sources (e.g., Morgan & Edmunds 2003; Dwek et al. 2007). Additional physical mechanisms such as interstellar medium (ISM) dust growth and/or nonstandard initial mass functions may be required (the so-called "dust budget crisis"; e.g., Rowlands et al. 2014). More precise dust mass constraints for unbiased samples of SMGs are needed to further investigate this issue. Another matter of debate in the community is what drives the intense star formation activity in SMGs: whether it is a mode of enhanced star formation efficiency, driven by major mergers (e.g., Hayward et al. 2011), and/or a more modest star formation efficiency driven by secular evolution in large disks with high gas fractions (e.g., Davé et al. 2011). One way to disentangle these two evolutionary modes proposed for SMGs is to compare the observed SFRs with the mass of gas available to form stars, which, until we have CO observations for large samples, can be roughly inferred from the dust mass (assuming $M_{\rm gas}/M_{\rm dust}$; Scoville et al. 2014, 2016, 2017; Groves et al. 2015; Kaasinen et al. 2019). The estimations of both dust and gas masses rely on the assumption that for SMGs the dust emissivity index (β, which describes the wavelength dependence of the dust emissivity per unit mass) is similar to what is measured in the Milky Way and other local galaxies, i.e., $\beta \simeq 1.5$–2.0 (e.g., Galliano et al. 2018). However, β has only been directly measured in small samples of SMGs using observations at the long enough wavelengths needed to break the intrinsic degeneracy between β and the cold dust temperature (e.g., Birkin et al. 2021; see also previous efforts with Herschel and AzTEC; Chapin et al. 2009; Magnelli et al. 2012).

To provide constraints on the dust emissivity index and temperature, we use ALMA to perform a systematic study of the 2 mm emission of a complete sample of 870 μm selected SMGs. First detected as part of the APEX LABOCA 870 μm survey of the Extended Chandra Deep Field South, LESS (Weiß et al. 2009), our sample is taken from the ALMA Cycle 0 follow-up program (ALESS), in which we observed 122 of the LESS sources at high sensitivity and spatial resolution through snapshot

observations at 870 μm in Band 7 (Hodge et al. 2013; Karim et al. 2013). The high resolution of the ALMA observations deblended multiple sources that were previously misidentified as single sources and located the SMGs to within 0$\farcs$3 (Hodge et al. 2013). These ALESS observations yield a sample of 99 robustly identified SMGs, a sample large and reliable enough to enable a complete and unbiased multiwavelength study of the properties of this galaxy population (e.g., Simpson et al. 2014; da Cunha et al. 2015; see also recent similar efforts in the UDS and COSMOS fields; Simpson et al. 2017, 2020; Stach et al. 2018; Dudzevičiūtė et al. 2020). In this paper, we present the first systematic (i.e., resolved) comparison of the 2 mm emission of a 870 μm selected sample, with which we characterize the long-wavelength SEDs and derive robust dust properties for individual SMGs.

This paper is organized as follows. In Section 2, we describe our ALMA Band 4 imaging of the ALESS SMGs. In Section 3, we obtain and analyze 2 mm flux measurements and compare them with the 870 μm properties of our sources. In Section 4, we derive the dust properties of our sources by fitting their observed SEDs using simple dust models. In Section 5, we discuss the robustness of our constraints, discuss selection effects, and compare the dust emissivities derived for our SMGs with other measurements and theoretical predictions. We provide a summary and conclusions in Section 6. Throughout the paper, we use a concordance ΛCDM cosmology with $H_0 = 70\,{\rm km\,s^{-1}\,Mpc^{-1}}$, $\Lambda = 0.7$, and $\Omega_m = 0.3$ (e.g., Planck Collaboration et al. 2020).

2. ALMA Band 4 Observations of SMGs

2.1. Observations

Our ALMA Band 4 continuum observations were carried out between 2015 December 26 and 2016 January 1, as part of the Cycle 3 Project #2015.1.00948.S (PI: E. da Cunha).

We targeted the 69 LESS fields that contain at least one MAIN catalog (i.e., most reliable) source from the Cycle 0 ALESS observations at 870 μm (Hodge et al. 2013) and centered each pointing on the brightest source in each field. Thanks to the multiplicity of the single-dish-detected LESS sources, 24 of our 69 LESS fields contain multiple SMGs identified in the Cycle 0 observations by Hodge et al. (2013), resulting in a total of 99 MAIN ALESS sources in our target fields, as well as 32 additional SUPPLEMENTARY catalog sources. At the frequency of our observations, the primary beam of ALMA is 40$\farcs$7, ensuring that, when centering each field on the brightest ALESS source, the remaining ALESS sources within the $\simeq$18$''$ 870 μm primary beam were covered by our pointings.

Our observations were taken in Band 4 (at a representative frequency of 152 GHz) using the total 7.5 GHz bandwidth available for continuum observations. Between 34 and 41 12 m antennas were used in the most compact array configuration in Cycle 3 (C34-1), with baselines ranging from 15 to 310 m. This antenna configuration was sufficient to achieve our desired resolution of 2$\farcs$3, which allows us to separate the different sources in fields where there are multiple ALESS SMGs, while not resolving out each individual source (based on their typical sizes of $\lesssim$0$\farcs$5; Simpson et al. 2015; Hodge et al. 2016). The weather conditions were adequate for Band 4 observations (precipitable water vapor between 1.35 and 3.82 mm). The quasar J0334$-$4008 was used for atmospheric, bandpass, flux, and pointing calibration, and J0348$-$2749 was used as a phase
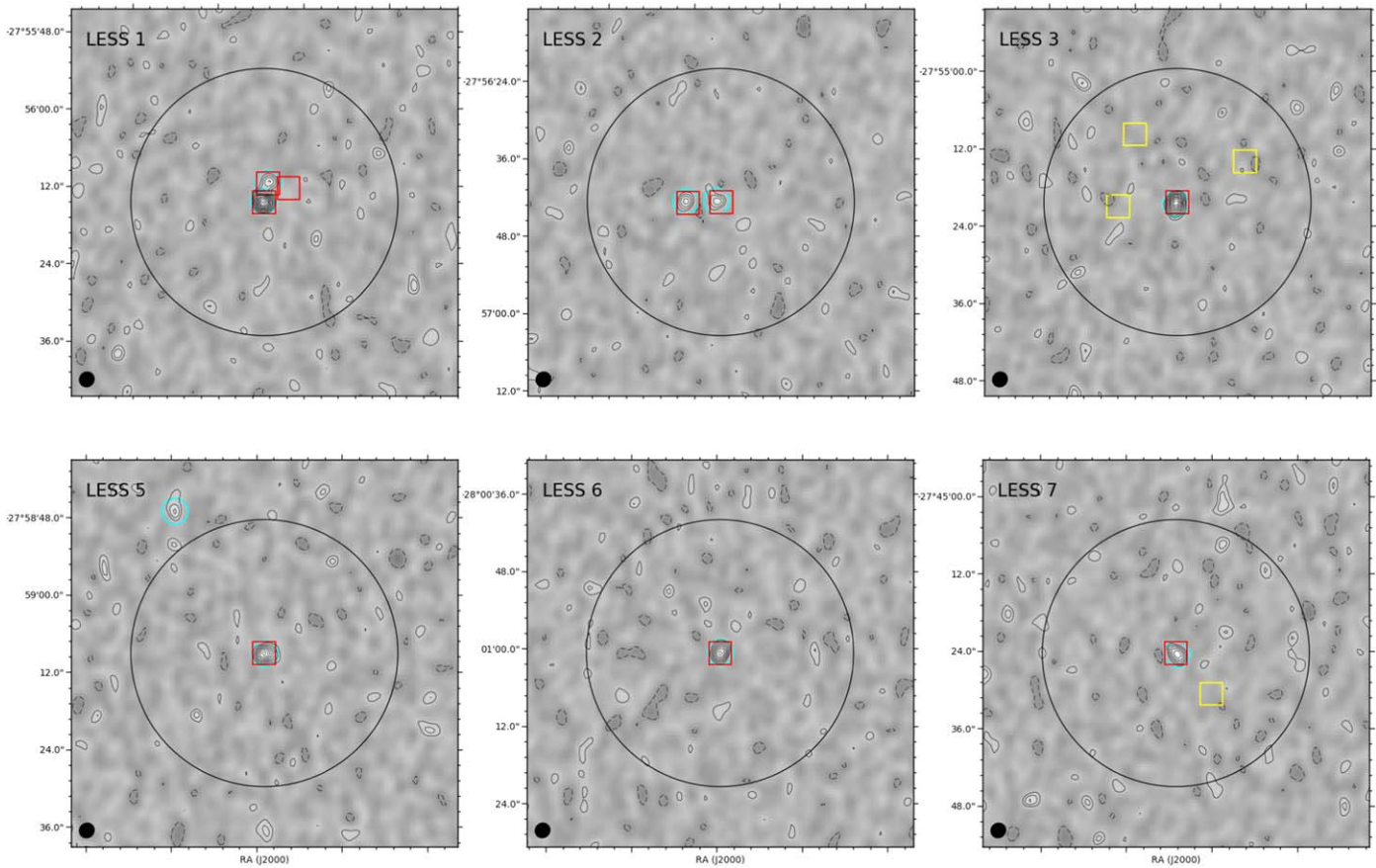
Figure 1. ALMA Band 4 (2 mm) maps of our first six fields. The contours show flux density levels starting at $\pm2\sigma$ and increasing in steps of 1σ, where σ is the rms noise measured in that map. The large black circle shows the primary beam FWHM ($\sim40''$), and the small black filled circle in the lower left corner shows the synthesized beam ($\sim2\rlap{.}''3$). Cyan circles indicate detections with S/N $\geqslant 4$, and squares indicate the positions of known ALESS sources detected at 870 μm by Hodge et al. (2013) (red for main catalog sources, yellow for supplementary sources).

calibrator. ALESS045.1 was also used as an atmospheric calibrator. Each of our 69 target fields was observed for 160 s.

2.2. Data Reduction and Imaging

The observations were processed using the ALMA automated data reduction pipeline in the Common Astronomy Software Application (CASA) version 4.5.1 and checked by the ALMA data quality assessment team. We verified that the pipeline produced high-quality data, and therefore we use the data as delivered by ALMA.

We generate images from the ALMA visibilities using the CLEAN task in CASA. CLEAN performs a Fourier transform to map the uv visibilities onto the image plane on the sky, producing a "dirty image." This image is then deconvolved from the point-spread function (i.e., the synthesized "dirty" beam) using the CLEAN algorithm (Högbom 1974) with robust (Briggs) weighting of the visibilities; we adopt `robust = 0.5`. The average rms obtained in our clean images is $\sigma = 53 \pm 2\,\mu$Jy beam^{-1} (with the error representing the standard deviation of the noise among all the maps), and the average beam is $2\rlap{.}''4 \times 2\rlap{.}''3$. This corresponds to a physical resolution of ~18 kpc at $z \sim 1$–3, the typical redshift range of our sample (da Cunha et al. 2015; Danielson et al. 2017). In Figure 1, we show the final cleaned ALESS Band 4 continuum images obtained using this procedure for the first six fields. Each image is $166'' \times 166''$, with a pixel scale of $0\rlap{.}''46$. The noise and beam properties of all 69 maps are uniform. All the maps are good quality with rms below our 60 μJy beam^{-1} request and fairly

circular beam (the beam axis ratio varies between 1.05 and 1.11); therefore, we use all the maps in a common source extraction step in the next section.

3. 2 mm Properties and Comparison with 870 μm Fluxes

3.1. Source Extraction and Catalog Matching

We detect sources in our cleaned continuum images using CASA. First, we identify sources with fluxes above 4σ in the maps using the BOXIT task, which searches the images to find contiguous sets of pixels above the given threshold and defines a rectangular box containing those pixels. Then, we use the IMFIT task to fit one or more two-dimensional Gaussian functions to the sources detected in each region defined by BOXIT. For each source, IMFIT returns the peak intensity, the location of the peak pixel on the image, the major and minor axis and position angle, and the total (integrated) flux. For unresolved sources, the peak flux and the total flux are the same, and the size and shape of the source match the synthesized beam.

Our source extraction procedure yields a total of 53 detections of ALESS main catalog sources with signal-to-noise ratio (S/N) $\geqslant 4$ within the primary beam FWHM (i.e., sensitivity >50% of the maximum). For these bright, "blindly" extracted sources, the positions in Band 4 agree very precisely with the previous Band 7 positions cataloged in Hodge et al. (2013), with only minor offsets of δR.A. $= 0\rlap{.}''07 \pm 0\rlap{.}''05$ and δdecl. $= 0\rlap{.}''07 \pm 0\rlap{.}''04$. We define a "well-sampled subset" of

27 sources for which we detect the 2 mm emission at S/N $\geqslant$ 4, which also have high-S/N detections at 870 μm and at 250 μm from Herschel/SPIRE (Swinbank et al. 2014), as well as spectroscopic redshifts from near-IR spectroscopy (Danielson et al. 2017), ALMA CO (Birkin et al. 2021), and [C II] (Swinbank et al. 2012). As we will see in Section 4.2, these are the sources for which we can constrain dust parameters robustly.

For sources below 4σ, since we have prior information based on the Band 7 data, we extract fluxes on their 870 μm positions. A total of 17 of those sources are detected with $1.5 \leqslant$ S/N < 4, allowing us to measure their fluxes. In Table 1 (Appendix A), we list the prior positions and 870 μm fluxes of our ALESS sources obtained with ALMA Band 7 (Hodge et al. 2013), along with our measured 2 mm Band 4 fluxes. All the fluxes are primary beam corrected (though note that in most cases the correction is unity because we centered our maps on the ALESS sources). Our sources are unresolved at our $\sim$2$\farcs$3 resolution. This is expected since most of the ALESS sources were unresolved in Band 7 with higher average spatial resolution (Hodge et al. 2013).

3.1.1. Flux Deboosting

We correct both our measured 2 mm flux densities and the Hodge et al. (2013) 870 μm flux densities for flux boosting due to Eddington bias and noise (note that we only correct the 2 mm flux densities of our blindly detected $\geqslant$4σ sources; sources for which we extracted fluxes at the prior 870 μm positions are not affected by flux boosting). We run simulations of this effect by injecting random sources into maps that have the same noise and synthesized beam properties as our Band 4 and Band 7 observations and then extracting their fluxes using the same method as for the data and comparing the original (deboosted) flux densities of our artificial sources with the recovered flux densities. We find that the flux boosting as a function of S/N is similar for both bands, and it follows the power law obtained by Geach et al. (2017). Therefore, we correct (i.e., deboost) the measured flux densities in both bands based on their S/N using $S_\nu^{\mathrm{deboosted}} = S_\nu^{\mathrm{measured}}/B$, where the boosting factor B is given by Equation (5) in Geach et al. (2017): $B = 1 + 0.2([\mathrm{S/N}]/5)^{-2.3}$. We provide the deboosted flux densities in Table 1 and adopt those values for all blindly extracted sources throughout the remainder of this paper.

3.1.2. Undetected Sources

A total of 29 of our 99 870 μm selected ALESS sources are undetected in the 2 mm maps, with no measurable flux at the position of the Band 7 detection (S/N < 1.5). Of those undetected sources (flagged with an asterisk in Table 1), seven lack photometric counterparts at any other wavelength except for 870 μm (Simpson et al. 2014; Swinbank et al. 2014), and they are typically low-significance detections at that wavelength (most are $\lesssim$4σ sources except for ALESS099.1, which is detected at $\sim$5σ; Hodge et al. 2013). These sources might be spurious sources in the Band 7 data; however, Karim et al. (2013) estimate that only 1.6% (i.e., 1 or 2) of the $\geqslant$3.5σ 870 μm sources should be spurious. They might instead be high-redshift ($z > 3$), high dust optical depth galaxies (da Cunha et al. 2015) with peculiar dust SEDs.

To further investigate the properties of our 29 undetected sources, we median-stack the 2 mm fluxes at the positions of the 870 μm detections. The stack produces no detection;

however, it allows us to place a 3σ flux density upper limit of 0.045 mJy.

3.1.3. 2 mm Sources with No Counterpart in the ALESS Main Catalog

Our source extraction procedure finds an additional sample of eight sources that are detected with S/N $\geqslant$ 4 within primary beam (PB) > 0.3, which we list in Table 2 (Appendix A). Since these are blindly extracted sources, we correct their measured fluxes for boosting using the method described in Section 3.1.1. All but two of these sources fall outside the primary beam of the ALMA 870 μm observations. Following the method described in Hodge et al. (2013) and Karim et al. (2013), we estimate the fraction of spurious sources in our data with S/N $\geqslant$ 4 to be less than 10%, and the corresponding completeness is 96%. We find that four of these sources have a robust Spitzer/IRAC 3.6 μm counterpart (within 0$\farcs$5) in the ECDFS IRAC-selected catalog of Damen et al. (2011), confirming that they are likely to be real galaxies. The remainder are still within the footprint of that catalog but have no counterpart within 1$''$, meaning that they would have an IRAC 3.6 μm magnitude fainter than the 5σ detection limit of the catalog, $m_{\mathrm{AB}} = 23.8$. They could be spurious or optically faint SMGs with very low 870 μm-to-2 mm flux ratios, either because they are at very high redshifts or because they have very cold dust or unusual dust properties such as low dust emissivity indexes (Section 3.4; see also Wardlow et al. 2018).

3.2. Comparison with Predicted Fluxes and 870 μm Fluxes: Why Are So Many Sources Undetected at 2 mm?

In da Cunha et al. (2015), we developed and used the "high-z extension" of the MAGPHYS SED modeling code (da Cunha et al. 2008) to fit the observed ultraviolet to radio emission of all 99 ALESS main catalog sources. The best-fit model SED of each galaxy was used to estimate the expected 2 mm flux in preparing our ALMA observations. In Figure 2(a), we compare those predicted 2 mm fluxes, scaled down by the 870 μm boosting factor (Section 3.1.1), with our measured fluxes. Overall, the predicted and measured fluxes are well correlated, and for the vast majority of sources for which we can extract a flux, they agree within a factor of two. Our 2 mm nondetections deviate the most from the predicted fluxes and had the largest 870 μm boosting factors ($B = 1.36 \pm 0.10$ on average). Therefore, flux boosting in the original 870 μm fluxes can explain our nondetections at least in part. Accounting for 870 μm flux boosting, the median predicted flux of our 29 nondetections drops from 152 to 103 μJy, still about a factor of two higher than our 3σ stack upper limit.

In Figure 2(b), we compare the 2 mm and 870 μm flux densities. The dispersion is significant at low S/N, but for the brightest sources they are very well correlated. However, our 2 mm nondetections seem to have a deficit in 2 mm flux density compared with the 870 μm flux density (even after accounting for 870 μm flux boosting). This may indicate different dust emission properties, redshift distributions, or selection effects. We analyze the 870 μm-to-2 mm flux ratios in more detail in Section 3.4.

We note that the flux ratio between two (sub)millimeter bands is sometimes used to infer the dust emissivity index directly (e.g., Aravena et al. 2016; González-López et al. 2019). A constant flux ratio between two bands (independent of redshift and dust temperature) is predicted if the two bands sample the low-frequency Rayleigh–Jeans (RJ) tail of the dust emission. If we use
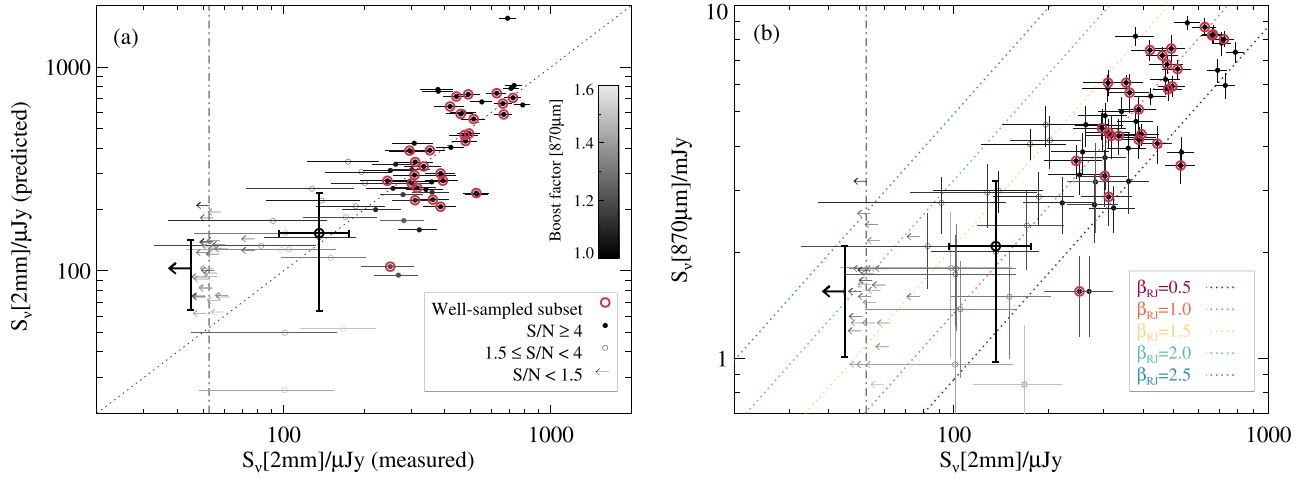
Figure 2. (a) Comparison between the measured 2 mm fluxes of our sources and the predicted MAGPHYS fluxes (da Cunha et al. 2015). The dotted line shows the identity. Each data point is color-coded according to the boosting factor of the 870 μm observations (Section 3.1.1). The predicted and observed fluxes are well correlated, and the vast majority of our sources have measured fluxes within a factor of 2 of the predictions. We find that the largest deviations occur for faint sources, which had the largest boosting factors in the original 870 μm observations. This explains, at least in part, why we overpredicted their 2 mm fluxes. (b) Measured 2 mm vs. 870 μm flux densities. The lines show the relation between the fluxes in those two bands *assuming the RJ approximation*, for different values for the dust emissivity index β_{RJ} (see Appendix B for why that approximation is not appropriate at our observed frequencies). In both panels, the vertical dashed line shows the average sensitivity limit of our observations. The filled black circles represent our individual $\geqslant 4\sigma$ detections (of those, we highlight our "well-sampled subset"; see Section 3.1 for details), the thin open circles show marginal detections ($1.5 \leqslant S/N < 4$), and the thin arrows show upper limits for undetected sources. The thick open circle shows the median value for all 17 marginal detections (error bars are the standard deviation), and the thick arrow shows the upper limit for all 29 undetected sources derived from stacking.
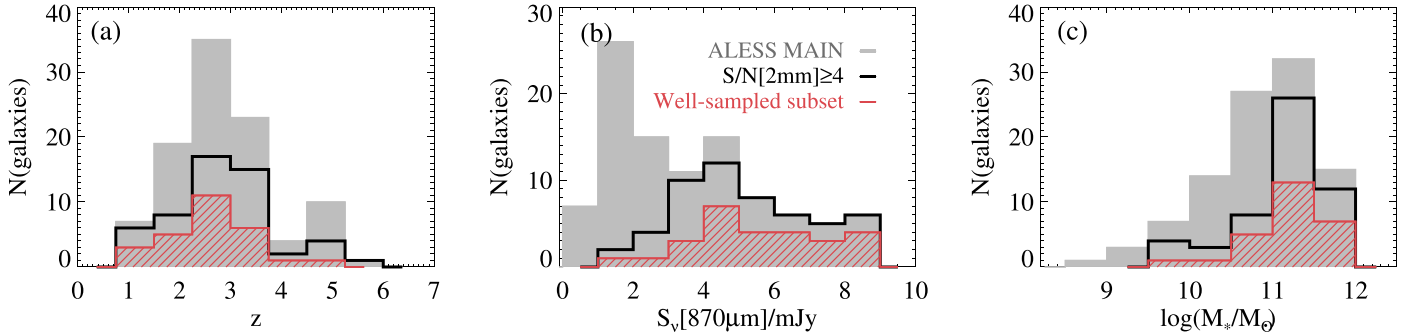

Figure 3. Properties of ALESS sources for which we measure a robust 2 mm flux with $S/N \geqslant 4$ (in black) and of those in our "well-sampled subset" (in red), compared with the properties of our full 870 μm selected sample (in gray): (a) redshift; (b) 870 μm flux density; (c) median likelihood estimates of stellar mass derived by fitting the full SEDs of the sources at fixed redshift (we choose the best available redshift for each target; 50/99 are spectroscopic redshifts from Swinbank et al. 2012; Danielson et al. 2017; Birkin et al. 2021), using the high-redshift extension of the MAGPHYS code (da Cunha et al. 2015).

the RJ approximation, the flux ratio depends on the dust emissivity index β_{RJ} alone (Equation (B2)). In Figure 2(b), we show the correlations between the 870 μm and 2 mm fluxes predicted in that regime, for different values of β_{RJ}. Those correlations are roughly parallel to our observed correlations, and a $\beta_{RJ} \simeq 1$ seems to match our observations; however, that does not necessarily mean that β_{RJ} is the true emissivity index of our sources. In Appendix B, we demonstrate that those values are unlikely to correspond to the real emissivity index in our sources because the RJ approximation is not valid for our observed bands at the redshifts of the ALESS SMGs, and more sophisticated modeling of the dust emission is needed (Section 4.1).

3.3. Properties of Detections versus Nondetections

The properties of the 99 ALESS main SMGs are described in detail in Hodge et al. (2013), Swinbank et al. (2014), Simpson et al. (2014), da Cunha et al. (2015), and Danielson et al. (2017). Here we use some of those known properties to investigate what

kinds of sources are most likely to be detected at 2 mm. Out of the 99 ALESS main catalog SMGs targeted in our 69 Band 4 fields, 53 (i.e., 54%) are detected above 4σ, which we consider to be very robust detections. In Figure 3, we plot the distribution of physical properties of our full 870 μm selected sample and of the subsample of targets for which we achieved robust ($\geqslant 4\sigma$) 2 mm detections. We find that the brightest 870 μm sources are all detected at 2 mm, with the detection rate falling steeply for sources below 4 mJy at 870 μm. This also means that we detect the sources with the highest dust masses, dust luminosities, star formation rates, and stellar masses (da Cunha et al. 2015). Interestingly, the redshift distribution of 2 mm bright sources follows the parent sample distribution closely, i.e., our detections do not seem to prefer a specific redshift range.

3.4. 870 μm-to-2 mm Flux Density Ratios

In Figure 4, we plot the distribution of 870 μm-to-2 mm flux density ratios for our ALESS sources. The 870 μm-to-2 mm ratios
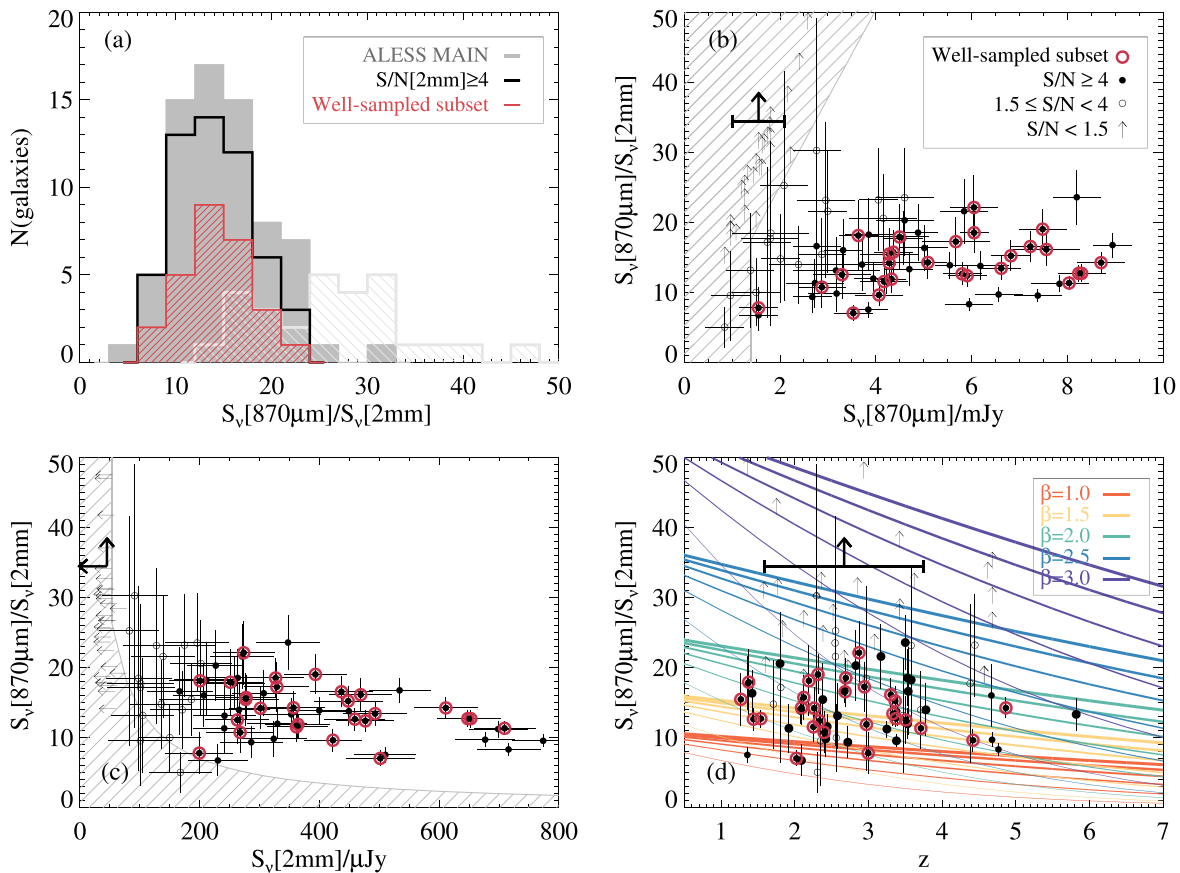
Figure 4. The 870 μm-to-2 mm flux density ratios, $S_\nu[870\,\mu\text{m}]/S_\nu[2\,\text{mm}]$, of our 870 μm selected SMGs. In panels (b)−(d) the symbols have the same meaning as in Figure 2. (a) Distribution of the flux ratios; the gray histogram shows the full ALESS main sample, including the distribution of upper limits for nondetections as the line-shaded histogram. (b) $S_\nu[870\,\mu\text{m}]/S_\nu[2\,\text{mm}]$ against 870 μm flux density. (c) $S_\nu[870\,\mu\text{m}]/S_\nu[2\,\text{mm}]$ against 2 mm flux density. (d) $S_\nu[870\,\mu\text{m}]/S_\nu[2\,\text{mm}]$ against redshift; the lines show the predicted ratios as a function of redshift for a set of isothermal, optically thin dust emission models with temperatures T_{dust} varying between 20 and 70 K (thin to thick lines) and emissivity indexes β varying between 1.0 and 3.0 (orange to purple). In panels (b) and (c) the shaded region shows the unobservable regions due to the preselection at 870 μm and the depth of our 2 mm observations. The 870 μm/2 mm colors span a relatively narrow range (their median 870 μm-to-2 mm flux ratio is 14 ± 5) and are weakly correlated with the 870 μm and 2 mm fluxes (though this could be due to selection effects) but uncorrelated with redshift. Panel (d) shows that we would expect a negative correlation with redshift for fixed dust temperature and emissivity index. Nondetections (S/N < 1.5) seem to have higher 870 μm/2 mm ratios, which would be consistent with higher T_{dust} and/or β.

of our strongly detected SMGs span a relatively narrow range. The median flux density ratio for the 70 SMGs for which we measure a 2 mm flux density is $S_\nu[870\,\mu\text{m}]/S_\nu[2\,\text{mm}] = 14 \pm 5$ (with the error indicating the standard deviation range; for the well-sampled subset, we find a median of 14 ± 4). For nondetections (S/N < 1.5), our 3σ stack upper limit implies ratios >34.5. Accounting for the upper limits for nondetections, the median flux ratio of the full ALESS sample increases to $S_\nu[870\,\mu\text{m}]/S_\nu[2\,\text{mm}] = 17 \pm 9$. We find weak correlations between $S_\nu[870\,\mu\text{m}]/S_\nu[2\,\text{mm}]$ and the flux densities at 870 μm and 2 mm, with Spearman rank correlation coefficients $r_S = 0.32$ (2.3σ) and $r_S = -0.36$ (2.6σ), respectively, although these correlations could be due to selection effects.

To put the 870 μm-to-2 mm flux density ratios into a more physical context, we compare them, in Figure 4(d), with the ratios predicted by simple, isothermal, and optically thin dust emission models with varying dust temperatures T_{dust} and emissivity indexes β, as a function of redshift. The models predict that $S_\nu[870\,\mu\text{m}]/S_\nu[2\,\text{mm}]$ should decrease with redshift, T_{dust}, and β, but the specific ratio for a given source is due to a combination of all these parameters. Our sources seem to span a broad model parameter space; however, this is sensitive to errors in the derived 2 mm flux density for the lower-significance detections, as well as

uncertainties introduced by photometric redshifts. Nevertheless, if we focus on only strong detections and our well-sampled subset (for which we have spectroscopic redshifts), we find that (i) we do not recover a strong redshift dependence ($r_S = -0.19$, < 1σ) and (ii) the location of these sources seems to favor models with $\beta \simeq 1$–2. The first finding indicates that perhaps the intrinsic dust properties of our SMGs depend on redshift (e.g., dust temperatures could be increasing at high redshift; see also Section 5.2), or more likely that selection effects are playing an important role (see Section 5.1). The latter finding appears to be in agreement with what is often assumed for the dust properties of galaxies, although the degeneracy between β and T_{dust} makes it difficult to estimate the actual dust emissivity index more precisely on a source-by-source basis using this ratio alone.

4. The Dust Properties of ALESS SMGs

To break the degeneracy between the dust temperature and emissivity index for our SMGs, we require additional observations sampling the dust SED closer to its peak.[17] In

---

[17] In Appendix B we demonstrate why simply assuming the RJ approximation is not appropriate for our data (and for other high-redshift ALMA observations).

this section, we describe our dust emission models and fits to the observed ALESS far-infrared/(sub)millimeter SEDs.[18]

4.1. Modeling the Dust Emission

The dust emission of a population of dust grains with equilibrium temperature $T_{\rm dust}$ is described by the general solution to the radiative transfer equation:

$$S_\nu \propto [1 - \exp(-\tau_\nu)]B_\nu(T_{\rm dust}), \qquad (1)$$

where $B_\nu(T_{\rm dust})$ is the Planck function and the optical depth τ_ν can be written as

$$\tau_\nu = \kappa_\nu \Sigma_{\rm dust}, \qquad (2)$$

where $\Sigma_{\rm dust}$ is the dust mass surface density and κ_ν is the frequency-dependent dust opacity, generally described by a power law,

$$\kappa_\nu = \kappa_0 \left(\frac{\nu}{\nu_0}\right)^\beta, \qquad (3)$$

where β is the dust emissivity index and κ_0 is the emissivity of dust grains per unit mass at a reference frequency ν_0. This function depends on the chemical and optical properties of dust grains (e.g., Draine & Lee 1984; Draine & Li 2007; Galliano et al. 2018). In this paper, we adopt $\kappa_0 = 0.77\,{\rm cm}^2\,{\rm g}^{-1}$ at $\nu_0 = 353\,{\rm GHz}$ (i.e., $\lambda_0 = 850\,\mu{\rm m}$), to be consistent with da Cunha et al. (2008, 2015).

For simplicity, throughout the remainder of this paper we assume isothermal dust models. Realistically, dust grains in galaxies are not at a single temperature; however, (optically thin) modified blackbody models have been shown to be a good approximation to the long-wavelength emission ($\lambda \gtrsim 100\,\mu{\rm m}$) caused by dust grains in thermal equilibrium, producing dust masses that are very close to the ones produced by more complex modeling that includes a distribution of temperatures (Draine & Li 2007), provided that consistent values for the dust emissivity are used (Bianchi 2013; see also, e.g., Lianou et al. 2019). Moreover, given the relatively low number of points sampling the dust emission of our sources, such simple isothermal models are the most complexity that can be afforded. Modeling the emission with multiple temperature components with varying emissivity indexes would result in a much larger number of free parameters than observational constraints, and the multiple dust parameters would be very difficult to constrain. This is also true for many other high-redshift sources observed in the dust continuum with ALMA, where often observations only in one or a few bands are available. Therefore, we adopt isothermal dust models and explore two cases: an optically thin approximation and a more general opacity scenario.

4.1.1. Optically Thin Approximation

Here we assume the simplest approximation for the dust emission in galaxies: optically thin dust, which means $\tau_\nu \ll 1$

---

at the observed frequencies, hence $[1 - \exp(-\tau_\nu)] \simeq \tau_\nu$, and the radiative transfer solution (Equation (1)) becomes

$$S_\nu \propto \Sigma_{\rm dust}\,\kappa_\nu B_\nu(T_{\rm dust}). \qquad (4)$$

In this case, the shape of the far-infrared/submillimeter dust SED, at fixed redshift, depends solely on the dust temperature $T_{\rm dust}$ and the emissivity index β. These two parameters can be strongly degenerate in the 870 μm-to-2 mm ratio, as shown in Figure 4(d). To break this degeneracy, we require additional observations sampling the dust emission closer to its peak. Figure 5 shows that in order to be sensitive to variations of both $T_{\rm dust}$ and β, we need to sample the dust SED in at least three bands, from the peak of the emission toward higher frequencies (which depends to first order on $T_{\rm dust}$) to the RJ tail at low frequencies (which mainly depends on β). Therefore, to sample the peak of dust emission, we use Herschel flux measurements when available (Swinbank et al. 2014). Of our sample of ALESS sources with robust (i.e., $\geqslant 4\sigma$) 2 mm measurements and $\geqslant 3.5\sigma$ 870 μm measurements, along with spectroscopic redshifts, 27 have at least one Herschel/SPIRE measurement at 250 μm: this constitutes our *well-sampled subset*. We focus on this subset in the remainder of the paper because for these sources we have the minimum set of bands needed to adequately sample the SEDs (Figure 5), and redshift uncertainties are not likely to affect our results.

4.1.2. General Dust Opacity

For completeness, we also explore the more general scenario where dust may remain optically thick toward far-infrared wavelengths. It is reasonable to consider that dust might be optically thick well into the far-infrared regime for very dusty sources such as SMGs (e.g., Conley et al. 2011; Simpson et al. 2017; Casey et al. 2019; Cortzen et al. 2020; Dudzevičiūtė et al. 2020). In this case, we use Equations (2) and (3) to define an additional parameter, the wavelength up until which the dust remains optically thick, i.e., $\lambda_{\rm thick}$, such that $\tau_{\lambda_{\rm thick}} = 1$. This $\lambda_{\rm thick}$ becomes an additional free parameter of the model, along with $T_{\rm dust}$ and β, and it depends on the intrinsic properties of the dust through its opacity function κ_ν and on dust mass surface density.

In the bottom panels of Figure 5, we show how varying $\lambda_{\rm thick}$ affects both the dust SEDs and the $S_\nu[870\,\mu{\rm m}]/S_\nu[2\,{\rm mm}]$ versus $S_\nu[250\,\mu{\rm m}]/S_\nu[870\,\mu{\rm m}]$ color space. This introduces a clear degeneracy: increasing $\lambda_{\rm thick}$ shifts the peak of the emission and affects the $S_\nu[250\,\mu{\rm m}]/S_\nu[870\,\mu{\rm m}]$ in the same direction as lowering the dust temperature. More detailed observations sampling the shape of the SED near its peak are needed to constrain all three parameters. Nevertheless, in order to account for the possibility that dust might not be optically thin at all wavelengths considered, we make an educated guess on $\lambda_{\rm thick}$. We assume a simple spherical shell geometry (e.g., Inoue et al. 2020), such that $\Sigma_{\rm dust} = M_{\rm dust}/4\pi R^2$, to investigate how $\lambda_{\rm thick}$ may vary as a function of dust mass and size for typical SMGs (Figure 6). In this simple case, $\lambda_{\rm thick}$ is given by

$$\lambda_{\rm thick} = \lambda_0 \left(\kappa_0 \frac{M_{\rm dust}}{4\pi R^2}\right)^{1/\beta}. \qquad (5)$$

As expected, for a fixed galaxy size, dust remains optically thick out to longer wavelengths as the total dust mass increases; at fixed dust mass, the dust column decreases and $\lambda_{\rm thick}$ becomes shorter as the radius increases. If we take the median dust mass of ALESS SMGs (and the 16th–84th percentile range of the sample dust
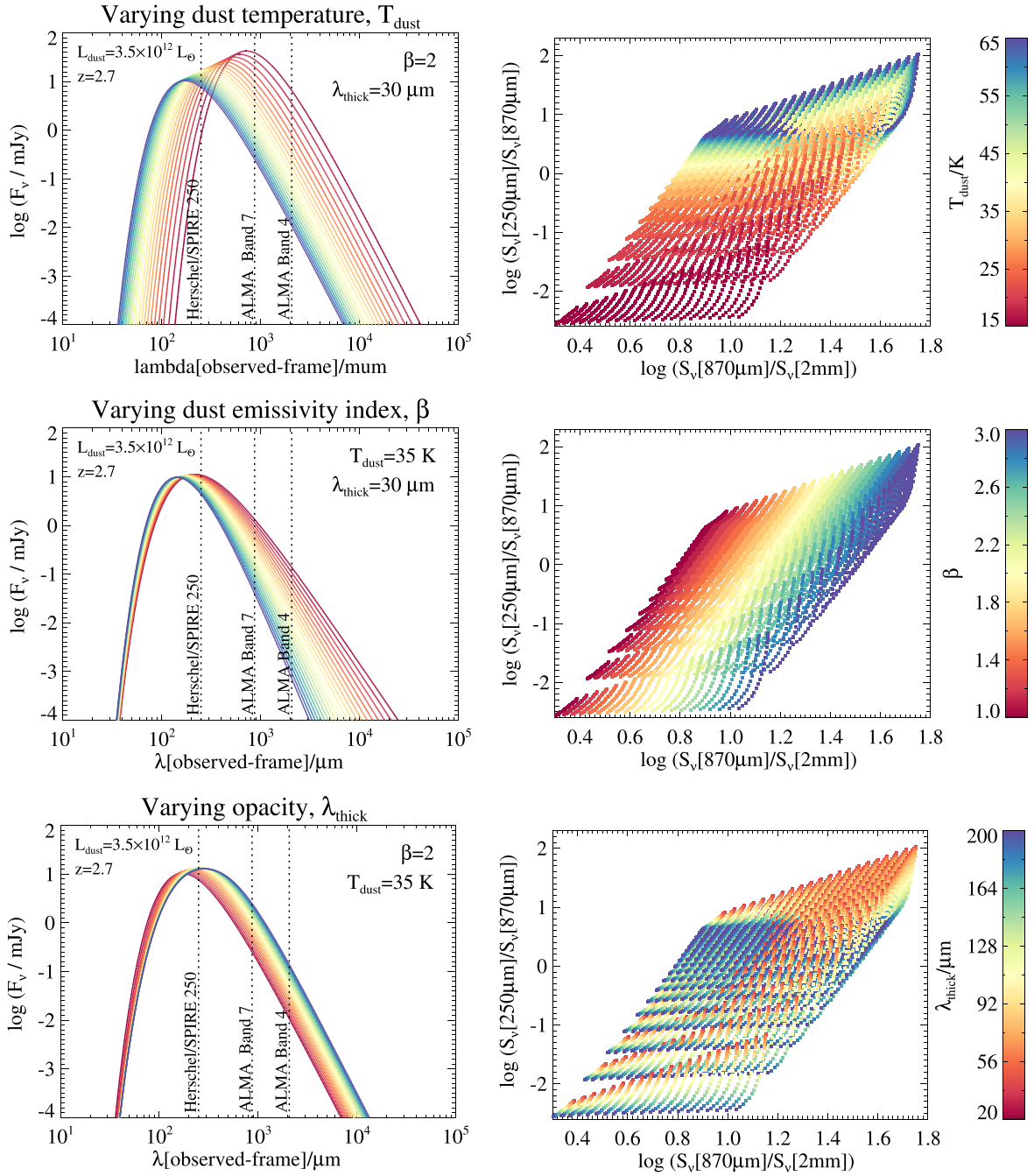
Figure 5. The predicted far-infrared colors of the dust emission in a galaxy at the median redshift of the ALESS sources ($z = 2.7$) and with their median dust luminosity ($L_{dust} = 3.5 \times 10^{12} L_\odot$; da Cunha et al. 2015), showing the effect of varying the dust temperature T_{dust} (top panels), emissivity index β (middle panels), and dust opacity, parameterized by the wavelength up until which dust remains optically thick, λ_{thick} (bottom panels; note that $\lambda_{thick} \lesssim 50$ μm approximates the optically thin case for the wavelength range sampled by our observations). The left panels show the effect of varying each parameter at a time on the global dust SED, while the right panels show the parameter space of galaxy colors varying all parameters at once, where we color-code each model by a single parameter at a time. Using a combination of at least three bands to sample both the peak of the SED and the RJ tail of the dust emission, we can form a color space where the variations of T_{dust} and β are approximately orthogonal at fixed λ_{thick} and therefore break the degeneracy between these two parameters. In the general opacity scenario where λ_{thick} is allowed to vary, T_{dust} and λ_{thick} remain degenerate with currently available observations.

mass distribution) derived by da Cunha et al. (2015) with MAGPHYS ($M_{dust} = 5.6^{+5.4}_{-3.4} \times 10^8 M_\odot$) and the typical radius measured by Hodge et al. (2016) using high-resolution ALMA observations in Band 7 ($R \simeq 2$ kpc), we obtain a typical $\lambda_{thick} \simeq 100 \pm 40$ μm (assuming for now a dust emissivity index $\beta = 2$; see also discussion in Simpson et al. 2017). This implies that, for the typical redshift of our sample ($z \simeq 2.7$), observations

shortward of ~ 370 μm (observed frame) are not necessarily in the optically thin regime, which affects the SEDs (Figure 5). In order to investigate systematic effects of the optically thin versus general opacity assumptions on the derived dust parameters, we fit our ALESS SEDs both with optically thin models and with a dust opacity model where we explore λ_{thick} in the range 60–140 μm, as indicated by our simple calculation above.
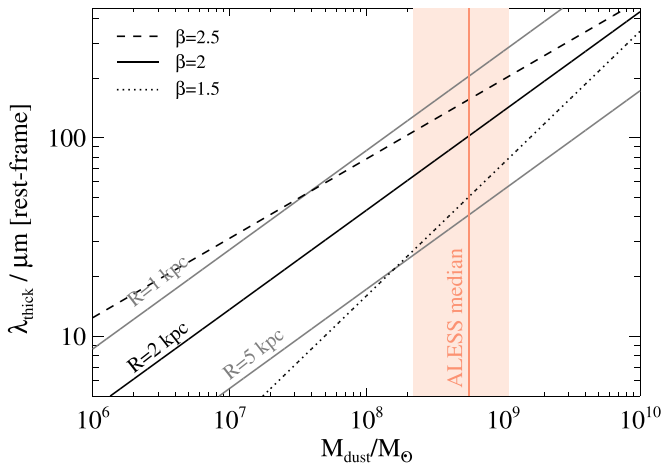
Figure 6. Wavelength up until which dust remains optically thick, λ_{thick}, as a function of total dust mass for different galaxy sizes and dust emissivity indexes (Equation (5)). The vertical orange line and shaded region show the median dust mass of ALESS SMGs computed by da Cunha et al. (2015) and the 16th–84th percentile of the dust mass distribution for the sample ($M_{\text{dust}} = 5.6^{+5.4}_{-3.4} \times 10^8 M_\odot$), which gives us a $\lambda_{\text{thick}} \simeq 100 \pm 40\ \mu\text{m}$ for the typical 2 kpc radius of the ALESS sources derived by Hodge et al. (2016), assuming $\beta = 2$.

4.1.3. SED Fitting Method

We use a Bayesian approach to fit the dust SEDs of our sources and recover posterior likelihood distributions for the free dust parameters: dust temperature (T_{dust}), dust emissivity index (β), dust luminosity (L_{dust}), and dust mass (M_{dust}). Since we assume isothermal dust, for each galaxy we only include observations sampling the SED at wavelengths longer than $70\ \mu\text{m}$ in the rest frame, as the effects of warmer dust components from stochastically heated dust grains are likely to impact the SEDs at shorter wavelengths. We generate a model library of dust SEDs with dust temperature T_{dust} uniformly distributed between 15 and 80 K and emissivity index β uniformly distributed between 1.0 and 3.0. For the general opacity case, we include λ_{thick} as an additional free parameter and distribute it uniformly between 60 and $140\ \mu\text{m}$, based on the calculation in the previous section. For each source at redshift z, we place the model dust SEDs in the observed-frame and apply the appropriate cosmic microwave background (CMB) corrections as described in da Cunha et al. (2013). We then compute the model fluxes in the Herschel/ SPIRE bands at 250, 350, and $500\ \mu\text{m}$ and in the ALMA Bands 7 and 4 (we also include ALMA Band 3 at 3.3 mm, available for 10 of our sources from Wardlow et al. 2018, and ALMA Band 8 at 0.63 mm, available for two sources from Rybak et al. 2019). We compare these model fluxes with the observed fluxes (and upper limits, when available) by evaluating the χ^2 goodness of fit of each model in the library. Then, we obtain marginalized likelihood distributions for all the free parameters.

4.2. Results: Dust Parameter Constraints

We start by focusing on the results obtained using the optically thin assumption, and then we compare with the results using the general opacity model using $\lambda_{\text{thick}} = 100 \pm 40\ \mu\text{m}$.

4.2.1. Results Using the Optically Thin Approximation

In Figure 7, we show an example of the outputs of our dust SED fitting for ALESS002.1, the brightest $870\ \mu\text{m}$ source in our well-sampled subset. For this galaxy, the SED is sufficiently well

sampled that both the dust temperature and emissivity index show well-constrained posterior likelihood distributions. Thanks to these two parameters being well constrained, the total dust luminosity and the dust mass are constrained to very small uncertainties as indicated by the narrow posterior distributions. The two-dimensional likelihood distributions allow us to explore parameter degeneracies in the fitting. As expected, and as discussed in the previous section and in numerous works in the literature (e.g., Shetty et al. 2009; Juvela et al. 2013), there is a strong degeneracy between T_{dust} and β that explains why, while these parameters are well constrained, the likelihood distributions are relatively wide.

In Figure 8 we show, for comparison, the results of fitting the dust SED of ALESS001.1, the brightest $870\ \mu\text{m}$ source, which also has a robust 2 mm detection but only Herschel limits. In this case, both T_{dust} and β are severely unconstrained, resulting in much broader likelihood distributions for the dust masses and luminosities. The strong degeneracies between the various dust model parameters become clear in the two-dimensional likelihood distributions. This demonstrates that the parameters derived from this fitting for galaxies with only ALMA Band 7 and Band 4 detections are not reliable, particularly T_{dust}, β, and M_{dust} (see also Appendix D). Therefore, in the remainder of this section, we focus solely on the well-sampled subset of 27 ALESS SMGs, accepting that these sources are not necessarily representative of the whole population (see Section 5.1). In Table 3, we present the median likelihood estimates of the dust temperatures, emissivity indexes, luminosities, and masses, as well as respective confidence ranges, obtained using the optically thin approximation for those 27 galaxies.

The precision of our constraints can be quantified by the width (i.e., the 16th–84th percentile range) of the posterior likelihood distributions. For our well-sampled subset, we constrain the dust emissivity index to within ± 0.25. This error on β depends strongly on the S/N in Band 4 and also to some extent in Band 7. The dust temperature T_{dust} is constrained to ± 5 K, and we achieve median precisions in dust luminosity and dust mass of ± 0.10 and ± 0.08 dex, respectively. We note that these are the median statistical errors on the fits within the context of assuming an optically thin model, and systematics associated with the choice of dust opacity are not included. We discuss possible systematic uncertainties by comparing with results from the general opacity fits in Section 4.2.2.

To analyze the distribution of physical properties of our sources, we show, in Figure 9, the stacked posterior likelihood distributions of β, T_{dust}, L_{dust}, and M_{dust}. We compare the results obtained for the well-sampled subset with those for the rest of the sample, which we include to check whether we can conclude something about those sources in a statistical sense. The individual posterior distributions for the sources that are not in the well-sampled subset may not contain much information; however, stacking them may reveal if any regions of the parameter space are preferred (as opposed to the completely unconstrained case, where we would retrieve our flat priors). These sources seem to peak at slightly lower temperatures; however, the probability extends to higher dust temperatures. Their dust luminosities and masses seem to be typically lower than for the well-sampled subset, as expected given their fainter submillimeter fluxes, and the emissivity indexes peak at similar values, although we note that the stacked posterior is much flatter.
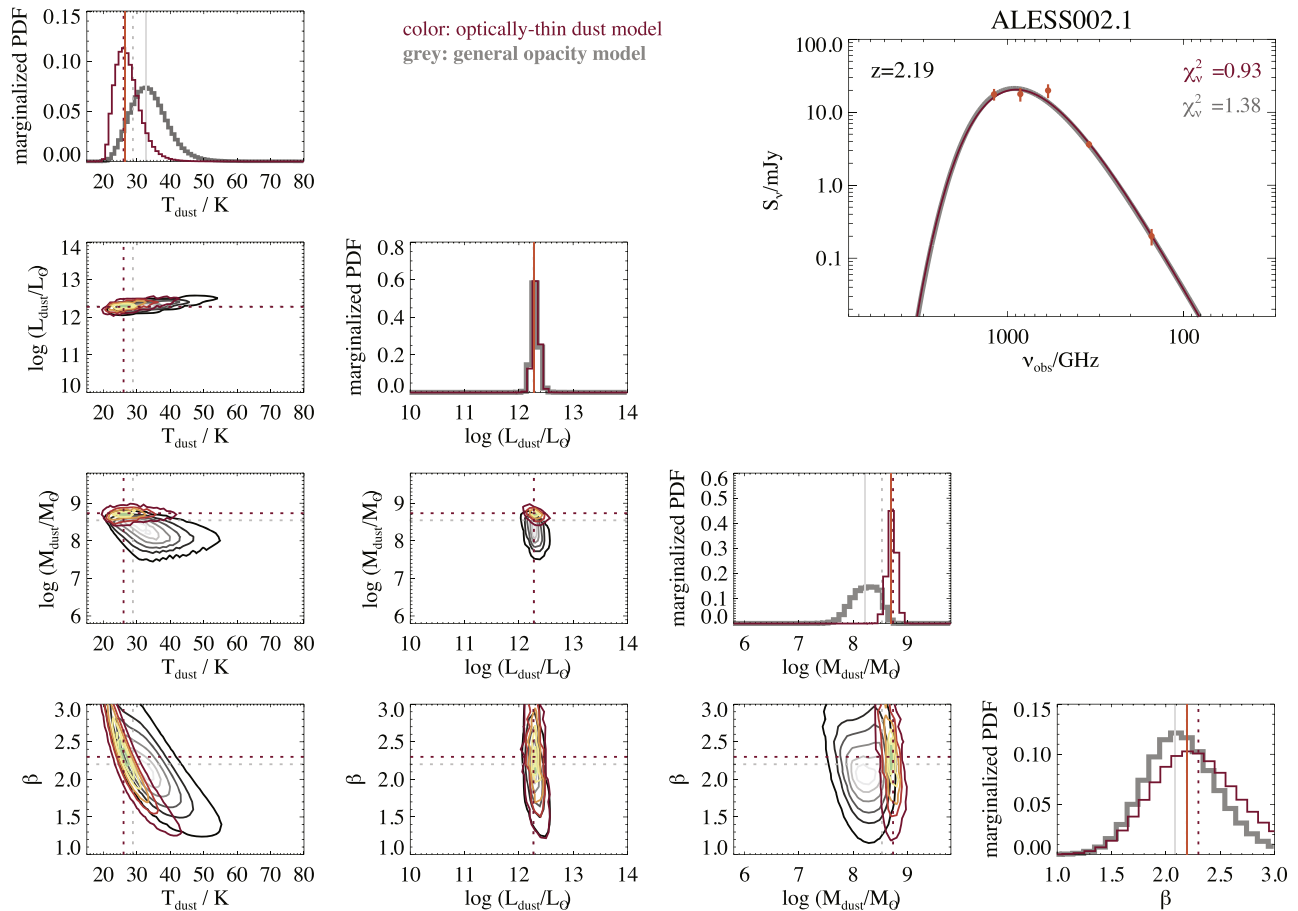
Figure 7. Outputs of our Bayesian dust SED fitting for ALESS002.1, the brightest source in our well-sampled subset. The top right panel shows the best-fit dust models (solid lines) and the observed fluxes (orange points). The remaining panels from top left to bottom right show the marginalized likelihood distributions for all the parameters in the fit: dust temperature (T_{dust}), luminosity (L_{dust}), mass (M_{dust}), and emissivity index (β), as well as the two-dimensional likelihood distributions of all combinations of these parameters. The contours show levels of equal probability: 1%, 10%, 25%, 50%, 75%, and 90% of the maximum probability value. The dotted lines indicate the best-fit parameters (i.e., corresponding to the minimum χ^2), and the vertical solid lines show the medians of the likelihood distributions. We plot the results for two fitting runs: the colored SED, histograms, and lines correspond to the optically thin dust model; the grayscale ones correspond to the general opacity scenario. For ALESS002.1, the best-fit SEDs in these two scenarios are virtually indistinguishable from each other, and the reduced χ^2 are very close (χ_ν^2 is actually smaller in the optically thin case because it produces a similarly good fit with fewer free parameters than the general opacity model). In the general opacity case, T_{dust} and M_{dust} are less well constrained owing to the additional degeneracy with λ_{thick}, and systematic offsets with the optically thin model are clear; the L_{dust} and β posteriors are very similar in the two cases.

For our well-sampled subset, we find median values of $T_{dust} = 30^{+14}_{-8}$ K and $\beta = 1.9 \pm 0.4$ for the stacked likelihood distributions (the errors are the 16th–84th percentile ranges of the stacked distributions). The emissivity indexes are consistent with typical values $\beta = 1.5 - 2.0$ measured in local galaxies and predicted by dust models (see Section 5.3 for a more detailed discussion).

Figure 10 shows that there is a negative correlation between the dust temperatures and emissivity indexes of our well-sampled sources ($r_S = -0.66$, 3.4σ) and a positive correlation between dust luminosity and temperature ($r_S = 0.73$, 3.7σ; a similar correlation is also found, e.g., by da Cunha et al. 2015). To check the robustness of these correlations, we also stack the joint posterior likelihood distributions, shown as contours. The fact that the peak of the stacked likelihood distributions follows the observed correlations between the median likelihood estimates shows that these correlations are robust.[19] This correlation

between T_{dust} and β could be caused to some extent by the intrinsic degeneracy between these two parameters; however, we show in Section 4.3 that our parameter estimates are accurate enough for these sources (because the data we use break the degeneracy), so it is likely that the correlation is real (see also Section 5.3).

4.2.2. Comparison with the General Opacity Model Results

In Figures 7 and 8, we also plot the results of our Bayesian fitting when using the general dust opacity model described in Section 4.1.2, allowing λ_{thick} to vary between 60 and 140 μm. In this case, the dust temperatures and dust masses are unconstrained even for our well-sampled subset, due to the strong degeneracy between T_{dust} and λ_{thick} (Figure 5): the widths of the likelihood distributions for these parameters are much larger than in the optically thin case. The best-fit model and median of the likelihood distribution of these parameters do not converge. This is another indication that the current observations are not sufficient to constrain a general opacity model where λ_{thick} is allowed to vary. More observations sampling the SED peak and measurements of the size of the dust emission region would help constrain

---

[19] The median likelihood estimate can be deceiving if a parameter is unconstrained: in that case the median will be the median of the prior, but the posterior would show that the parameter is unconstrained because it would resemble the prior, in our case, a flat distribution.
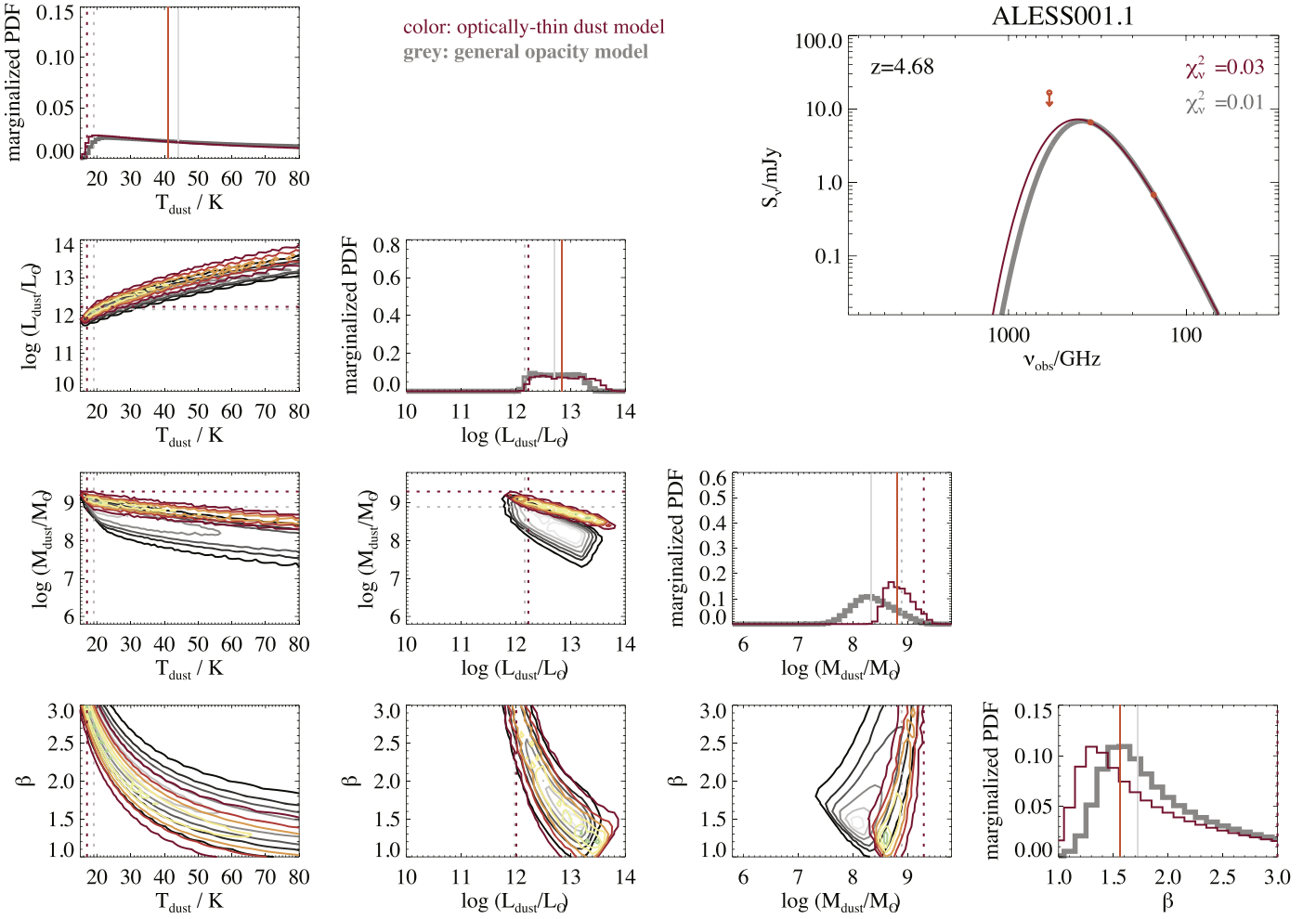
Figure 8. Similar outputs of our fitting to those in Figure 7, but for ALESS001.1, a source without Herschel measurements (only upper limits). Since there are no measurements at frequencies higher than Band 7 to sample the peak of the dust emission, T_{dust} and β are poorly constrained, and consequently the errors on L_{dust} and M_{dust} are also much larger (wider likelihood distributions) compared to ALESS002.1. Because of the lack of data, strong degeneracies between the model parameters become evident in the two-dimensional likelihood distributions, even in the optically thin case.

this parameter more precisely. With the current data, while the quality of the SED fits is comparable between the optically thin approximation and the general opacity model, these two different modeling assumptions can lead to large differences in the inferred dust temperatures and, consequently, the dust masses.

We also compare the stacked likelihood distributions obtained using the general opacity model for our well-sampled subset in Figure 9. In this case, the dust temperatures are more poorly constrained even for the ensemble of 27 well-sampled galaxies (due to the degeneracy with λ_{thick}) but tend to peak at higher values. The dust masses tend to be lower than in the general opacity case, due to the higher T_{dust}. The recovered dust luminosities are very similar to those in the optically thin scenario, and, importantly, so are the dust emissivity indexes. This shows that our estimates of β for this subsample are robust regardless of whether an optically thin or general opacity scenario is adopted.

In Figure 11, we compare the median likelihood estimates of dust physical parameters derived using the optically thin assumption with those derived using the general opacity model. The parameters are well correlated; however, we find strong systematic offsets in the derived dust temperatures: the general opacity scenario produces T_{dust} typically $\sim$10 K warmer than the optically thin case (see also Simpson et al. 2017). This leads

to a strong offset in the inferred dust masses, which are typically 0.5 dex (i.e., a factor of 3) lower in the general opacity scenario than in the optically thin case (the same offsets are also seen in the medians of the stacked likelihood distributions in Figure 9). These differences can have very strong implications when interpreting inferred dust masses in the context of chemical evolution and dust production models, especially at high redshift, where current models required substantial ISM growth to account for large inferred dust masses (e.g., Rowlands et al. 2014; Mancini et al. 2015; Dudzevičiūtė et al. 2020, 2021). Nevertheless, we find that the inferred dust luminosities and emissivity indexes seem quite robust against dust model assumptions, with no systematic offsets. We checked that these differences would be more pronounced if we chose to include models where the dust remains optically thick beyond 140 μm. However, in that case, the parameters with the highest systematic offsets, T_{dust} and M_{dust}, would remain almost unconstrained with the current data owing to the strong degeneracy with λ_{thick}; therefore, the systematic offsets would be mostly a result of the prior. Given our calculation in Section 4.1.2, very high values of λ_{thick} seem unlikely (though see Riechers et al. 2013, who claim $\lambda_{thick} \simeq 200\,\mu$m in high-redshift, lensed SMGs). We caution that very optically thick dust could lead to even more
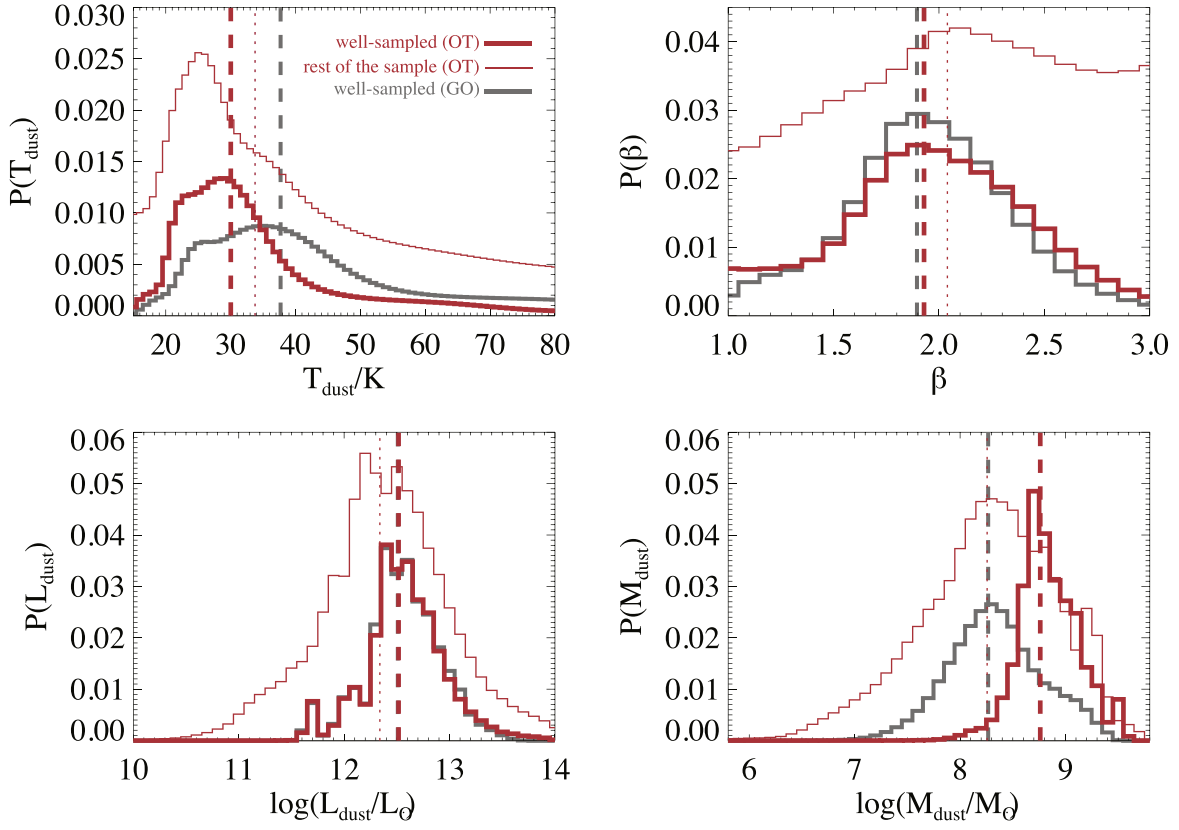
Figure 9. Stacked likelihood distributions of the dust parameters for the ALESS sample. The red histograms show the results of fitting the SEDs using the optically thin (OT) assumption: the thick line corresponds to the 27 sources in our well-sampled subset, and the thin line shows the stacked probability density functions of the remaining 72 sources. For the well-sampled subset, we find cold dust temperatures $T_{dust} \simeq 30^{+14}_{-8}$ K, emissivity indexes $\beta \simeq 1.9 \pm 0.4$, dust luminosities $\log(L_{dust}/L_\odot) = 12.5^{+0.4}_{-0.3}$, and dust masses $\log(M_{dust}/M_\odot) = 8.8^{+0.3}_{-0.2}$ (medians of the stacked likelihood distributions, errors given by the 16th–84th percentiles). In gray we show, for comparison, the stacked likelihood distributions for the well-sampled sources using the general opacity (GO) model, which shows offsets toward higher T_{dust} and lower M_{dust}. However, L_{dust} and β remain practically the same, meaning that the estimates of these parameters are robust against dust opacity assumptions.
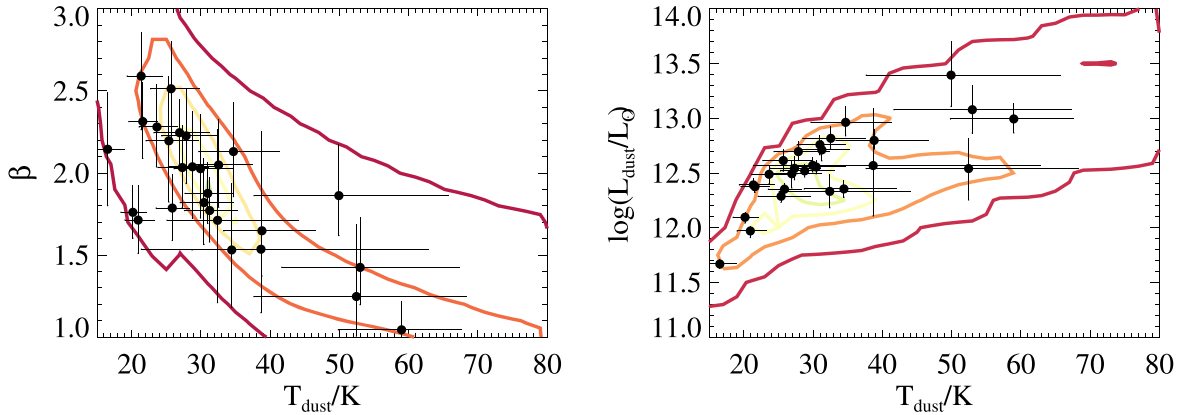
Figure 10. Relation between dust temperature and emissivity index (left panel) and dust luminosity (right panel) for the 27 sources in our well-sampled subset (optically thin case). The median likelihood estimates for each source are plotted as black circles, with the errors given by the 16th–84th percentile ranges of the likelihood distributions. The contours show areas of equal probability of the stacked joint likelihood distributions. We note that we find similar correlations in the general opacity scenario (though the correlations are shifted owing to the systematic offsets in T_{dust} described in Section 4.2.2).

significant differences in the inferred dust masses (factors of 10 and more).

We note that, with the available data, we cannot distinguish which of these scenarios, optically thin dust or general opacity with $\lambda_{thick} = 60\text{–}140\,\mu m$, is more likely: the best-fit model probabilities of the optically thin to general opacity scenario are very close. Given the expected dust masses and sizes

(Hodge et al. 2016; Gullberg et al. 2019), we expect the optically thick models to be appropriate at least for some of the sources. Nevertheless, in the following sections, unless otherwise stated, we will focus on the optically thin scenario, since these models are better constrained, and they are more widely used, thus facilitating comparisons with the literature.
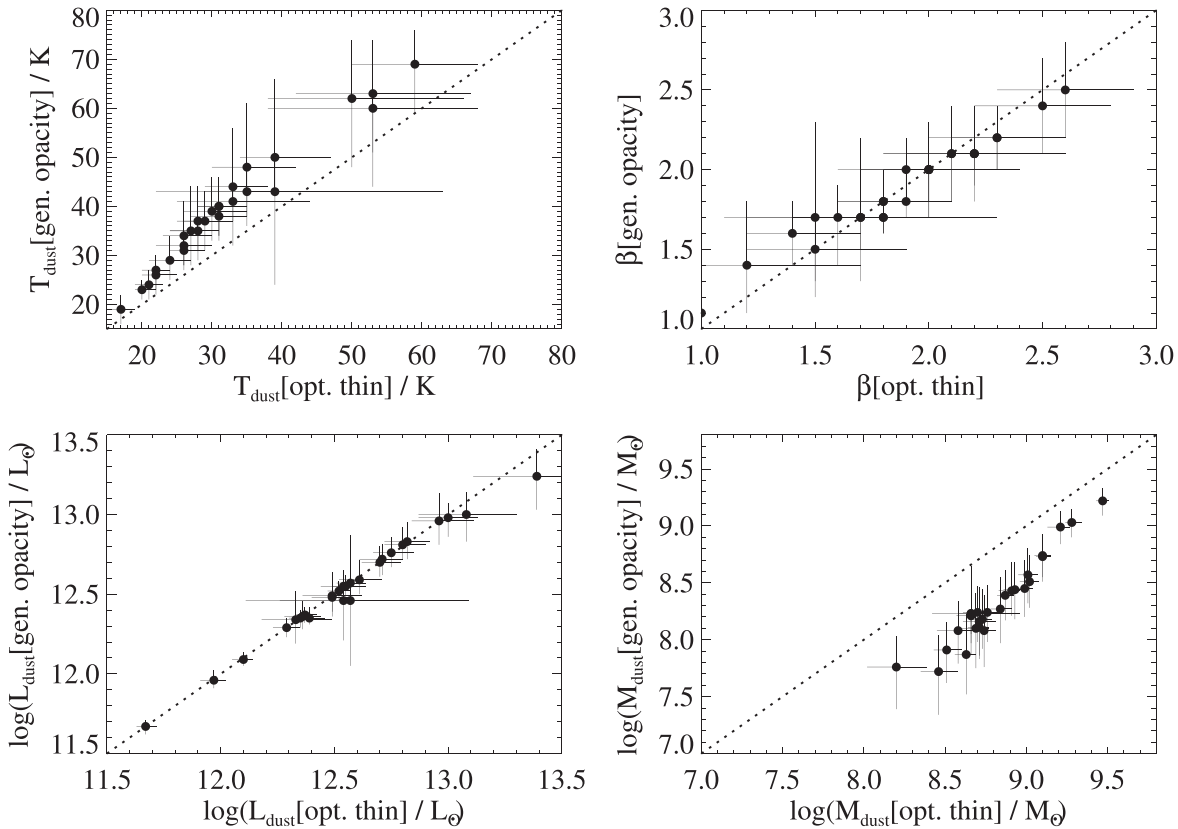
Figure 11. Comparison between the median likelihood estimates of dust temperatures (T_{dust}), emissivity indexes (β), luminosities (L_{dust}), and masses (M_{dust}) of our well-sampled subset of 27 ALESS SMGs when fitting their dust emission using optically thin dust models and a general opacity model with $\lambda_{thick} = 60$–$140\ \mu m$ (Section 4.1.2). In each panel, the dotted line represents the identity. The error bars are the 16th–84th percentiles of the posterior likelihood distribution for each source. The parameters derived using different model assumptions are well correlated; however, we find strong systematic differences in T_{dust} and M_{dust}. L_{dust} and β are robust against model assumptions on the dust opacity, as also shown in Figure 9.

4.3. Accuracy of Our Fitting Method

Before we move on to interpreting our results in a broader context, we must first establish the accuracy of our derived dust parameters. Previous studies focusing on modified blackbody fitting of the dust emission in compact galactic dust cores (e.g., Shetty et al. 2009; Juvela & Ysard 2012; Juvela et al. 2013) show that a correlation between T_{dust} and β can be introduced artificially to some extent by performing χ^2 minimization on noisy data. Bayesian methods such as ours are shown to produce more robust results (see also, e.g., Kelly et al. 2012) because they treat uncertainties rigorously and self-consistently, and as a result they do not produce spurious correlations between the parameters due to measurement uncertainties.

To address these issues in the context of this work, in this section we generate a suite of mock dust emission models to quantify the accuracy to which we expect the dust properties to be recovered from our fits. Again, we assume that dust emission in galaxies is isothermal and optically thin, and it can be described by simple modified blackbodies with dust temperature T_{dust} and emissivity index β (Equation (4)). We generate a library of 5000 models with dust temperatures uniformly distributed between 15 and 80 K, β between 1 and 3, and dust luminosity $\log(L_{dust}/L_{\odot})$ between 11.3 and 13.5 (a luminosity range similar to that of our SMGs; da Cunha et al. 2015). To simulate our observables, we place these models at different redshifts using a Gaussian distribution centered at $z = 2.7$, similar to the redshift distribution of our ALESS sources (Simpson et al. 2014; da Cunha et al. 2015). For each

model, we randomly draw a set of T_{dust}, L_{dust}, β, and z from these distributions, and we compute the predicted ("observed") flux of each model in the same bands as for our observations, i.e., the Herschel/SPIRE bands, ALMA Band 7 at 870 μm, and ALMA Band 4 at 2 mm. We include the effects of the CMB in the observed fluxes as prescribed in da Cunha et al. (2013). We then perturb these observed fluxes by $\pm 15\%$ to mimic our typical observational errors, and we assign observational uncertainties to each flux that are similar to those of our real observed galaxies. That is, we assume (i) a random S/N drawn between 4 and 6 in the SPIRE 500 and 350 μm bands and between 4 and 10 in the 250 μm band (Swinbank et al. 2014), (ii) a random S/N drawn between 3 and 15 in ALMA Band 4, and (iii) an ALMA Band 7 S/N that is correlated with the Band 4 S/N in the same way as our observations (which yields a distribution between 4 and 40).[20] We then fit our mock observations in the same way as we fit the actual observations in Section 4.1.

Figure 12 shows the accuracy of the derived dust properties of our mock observations. The input parameters are well recovered by our method for SEDs that have as many observational constraints as our well-sampled subset of ALESS sources. Our method typically recovers the input dust luminosities to ± 0.13 dex, the dust temperatures to within ± 6 K, the emissivity

---

[20] We note that, strictly speaking, the S/N should correlate with the actual model fluxes; however, we choose to set our simulation up this way because it allows us to perform the test with realistic errors but at the same time without limiting the parameter space of our models.
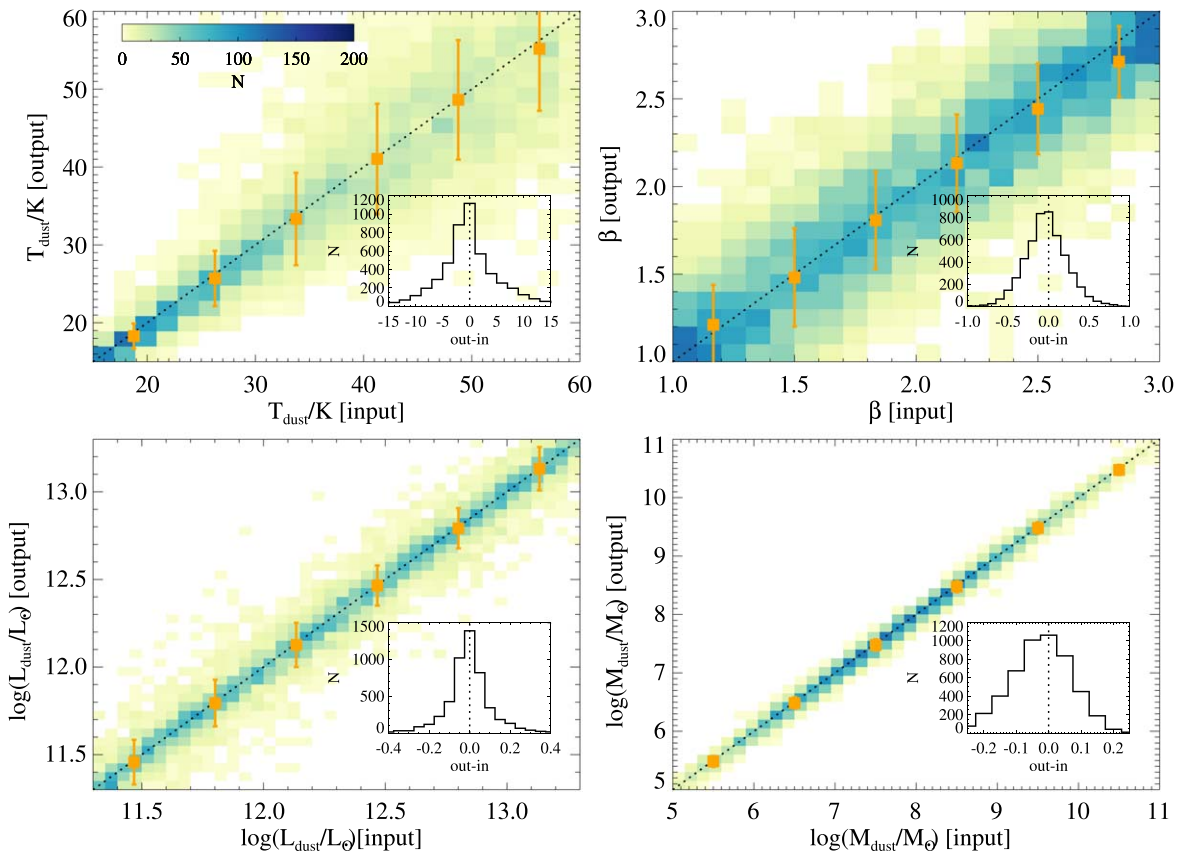
Figure 12. Accuracy of our fitting method in constraining the dust temperature (top left), emissivity index (top right), luminosity (bottom left), and mass (bottom right). For each of our 5000 mock models (described in Section 4.3), we plot the density of input parameter vs. output median likelihood estimate from our fitting. The black dotted line is the identity line, and the orange squares show the median in different bins, with the error bar showing the standard deviation in each bin. The insets show the overall distribution of the output value minus the input.

indexes to within ± 0.27, and the dust masses to ± 0.1 dex (these values are the standard deviations of the difference between input and output values). The systematics are minimal, with median offsets (i.e., difference between output and input values) of -0.007 dex for L_{dust}, -0.5 K for T_{dust}, -0.04 for β, and -0.017 dex for M_{dust}. It is worth noting that the accuracy of T_{dust} estimates decreases for higher temperatures, which is expected because the peak of the dust SED shifts to lower wavelengths and is less well sampled by the SPIRE bands. However, even in that regime the output values are still distributed around the input values (i.e., no significant systematics). The results of this test allow us to conclude that the dust parameters obtained for our well-sampled subset are robust, at least if assumptions about dust opacity are correct (see discussion below). We check that when we perform this test, we start with uncorrelated T_{dust} and β, and the results are also uncorrelated; therefore, we conclude that our found correlation between T_{dust} and β is not likely a result of fitting noisy data using our method. In Appendix D.1, we use similar simulations to show that our dust parameters would not be accurate enough if the fits did not include Band 4 data or Herschel data, which is why we chose to focus mainly on our well-sampled subset for which both are available.

It has to be noted that the self-consistency check described above assumes that we are using the correct model for the dust emission, but that may not be the case if, for example, dust is more optically thick than assumed. Therefore, in Appendix D.2 we test the accuracy of our derived parameters in the case where the input mock observations are generated using the general opacity model, but the models used to fit those

observations include only optically thin models. Figure 20 shows that, at least for the range of λ_{thick} explored (between 60 and 140 μm), no significant biases are found in β and L_{dust} when using the incomplete assumption of optically thin dust. However, not surprisingly, systematic offsets arise for T_{dust} (because this parameter depends on the peak of SED, which is most affected by the optical depth effects) and M_{dust} (because it depends strongly on T_{dust}). The offsets correlate strongly with λ_{thick}, in the sense that the longer λ_{thick} is the more the model deviates from the optically thin assumption, as well as with T_{dust}, since hotter dust peaks at shorter wavelengths and therefore is more affected by the dust opacity assumptions.

5. Discussion

5.1. Selection Effects

In the previous section, we show that our dust parameters are robust for our well-sampled subset (bar systematics due to opacity modeling assumptions), and therefore the measured correlation between T_{dust} and β is not likely introduced by our fitting method. In this section, we explore the impact of selection effects on our derived dust properties and their correlations. We use the library of (optically thin) dust models from the previous section, for which we have, for each dust model at a given redshift, the predicted fluxes in the Herschel and ALMA bands. Then, we apply the same flux selections to those models as in our observations. We apply two selections: (1) all models that would be detected above 4σ in our 2 mm observations ($\sigma = 0.053$ mJy beam^{-1}), plus $\geqslant 3.5\sigma$ detection in
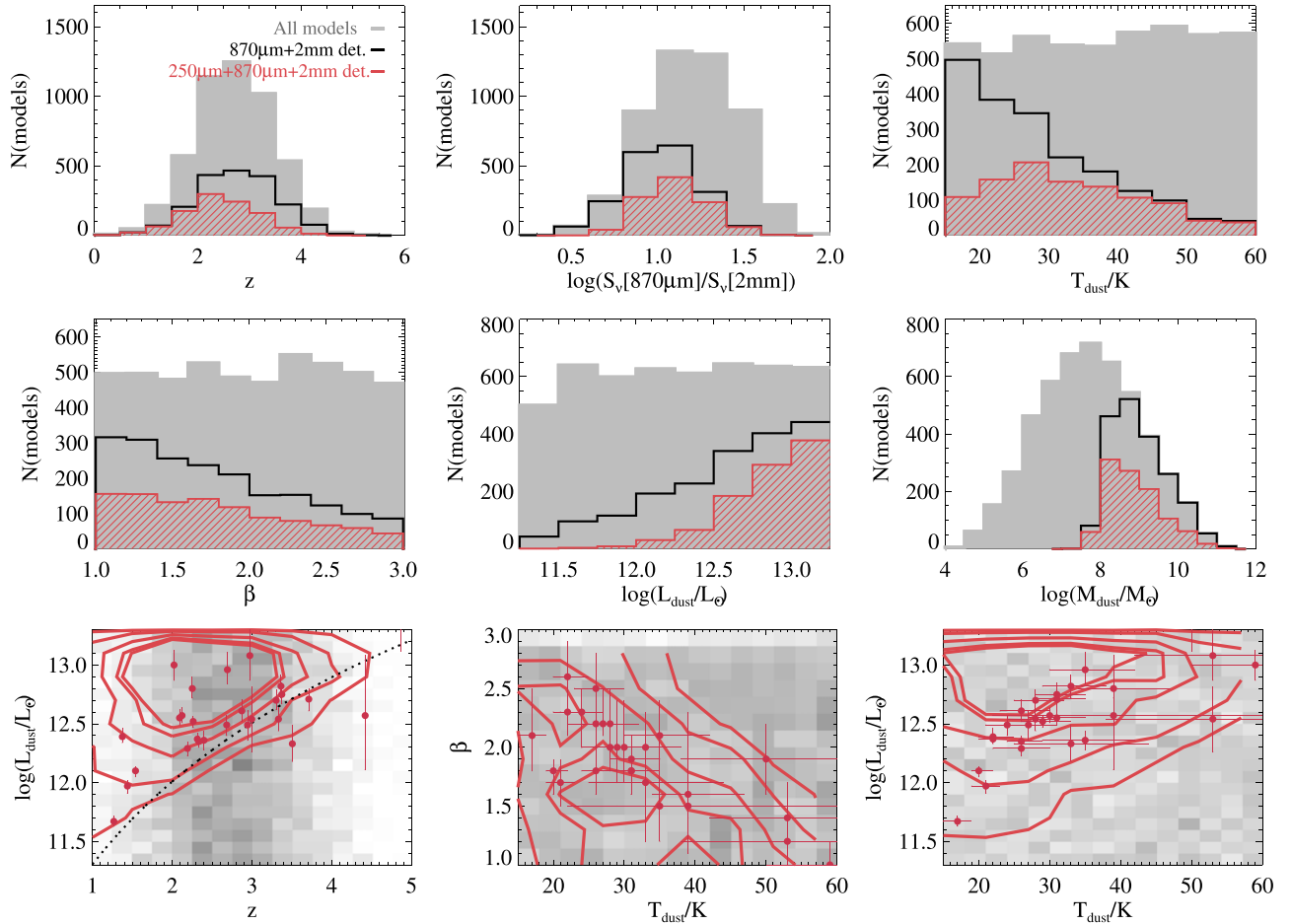
Figure 13. Distribution of physical parameters and observables in our library of dust models depending on our selection criteria. The model library was set up to have a similar redshift distribution to that of our ALESS SMGs and uniformly sample the dust temperature, emissivity index, and dust luminosity. Top and middle panels: the gray histograms show the full library of models, while the other two histograms show the effect of applying flux cuts similar to the ones in our ALESS observations. Black: $\geqslant 3.5\sigma$ detection in Band 7 (870 μm), where $\sigma = 0.4$ mJy beam^{-1} (Hodge et al. 2013), and $\geqslant 4\sigma$ detection in Band 4 (2 mm), where $\sigma = 0.053$ mJy beam^{-1} (this paper). Red: same as previous, i.e., strong detections in Bands 7 and 4, plus $\geqslant 4\sigma$ detection in Herschel/SPIRE at 250 μm, where $\sigma = 3$ mJy (Swinbank et al. 2014); this criterion is similar to the selection of our 27 "well-sampled" ALESS sources. Bottom panels: relation between physical properties in our library of dust emission models. The gray shading shows the density of models in the full library, showing that there are no a priori correlations between the physical parameters. The red contours show the distribution of models to which flux cuts mimicking the selection of our "well-sampled" subset have been applied. For comparison, we also plot median likelihood estimates of the properties of our well-sampled subset as red circles. The dotted line in the first panel shows a $\sim(1 + z)^4$ selection on luminosity; this is mostly imposed by the 250 μm flux cut.

Band 7 (870 μm), where $\sigma = 0.4$ mJy beam^{-1} (this is the original ALESS selection; Hodge et al. 2013); and (2) all models that would obey our "well-sampled" subset detection criteria, i.e., models that obey the previous criterion and that would have a $\geqslant 4\sigma$ detection in Herschel/SPIRE at 250 μm, where $\sigma = 3$ mJy (Swinbank et al. 2014).

Figure 13 shows that the first selection criterion (Band 4 and 7 detections) selects sources with higher dust luminosities, lower dust temperatures, and higher emissivity indexes: all these tend to boost the 2 mm flux. The result is that the models with the highest dust masses are selected (the 2 mm flux cut is effectively a dust mass selection; 870 μm is also close to a dust mass selection, as shown by Dudzevičiūtė et al. 2020). This flux cut also reproduces the typical 870 μm-to-2 mm flux ratio of our observations and the fact that we preferentially detect the brightest 870 μm sources. When the second criterion is applied (i.e., detections in Bands 4 and 7, plus at 250 μm), we tend to select models at lower redshifts, we lose a large fraction of low-T_{dust} models, and the β distribution becomes flatter. These changes are mainly caused by the 250 μm flux cut, which imposes a luminosity limit with redshift and selects

preferentially warmer dust. The resulting T_{dust} distribution looks similar to the stacked T_{dust} posterior for our well-sampled subset (Figure 9), peaking at about 30 K.

The bottom panels of Figure 13 show the relations between several physical properties in our model library and how they change when we apply our selection criteria for the well-sampled subset. These panels clearly show that our flux cuts exclude some regions of the parameter space, making a priori uncorrelated properties appear correlated for SMG samples when applying certain multiwavelength flux cuts, as illustrated by the red contours. Most notably we would not detect high-β, high-T_{dust} sources according to our selection, which could be affecting our derived β–T_{dust} correlation, at least to some extent. This is driven by the ALMA selection at 870 μm and 2 mm: imposing solely a 250 μm flux cut would retrieve models spanning the full T_{dust}–β parameter space of our library. We note that we would still detect low-β and low-T_{dust} sources, but the 250 μm flux cut means that it would be less likely, and indeed such sources do not seem to exist in our sample. Nevertheless, our models are more strongly correlated than the distribution of models shown by the red contours (with

Spearman rank correlation coefficients $r_S = -0.69$ and $r_S = -0.47$ for our well-sampled subset and the models, respectively), indicating that the correlation between T_{dust} and β is not necessarily caused only by the sample selection (the same can be said of the correlation between T_{dust} and L_{dust}, with Spearman rank correlation coefficients of $r_S = 0.73$ and $r_S = 0.17$ for our sources and the models shown in red, respectively).

5.2. Evolution in $S_\nu[870\,\mu m]/S_\nu[2\,mm]$?

In Section 3.4, we find very little evidence for evolving $S_\nu[870\,\mu m]/S_\nu[2\,mm]$ with redshift for the sources with robust 2 mm fluxes. Here we employ the empirical backward evolution model of Casey et al. (2018b) to test whether or not a nonevolving ratio of 870 μm to 2 mm would be expected in this ALESS data set. For example, if the S/Ns of individual detections are low, then an evolution in $S_\nu[870\,\mu m]/S_\nu[2\,mm]$ might not be observable unless the sample is sufficiently large. Alternatively, if there is substantial evolution in the average dust temperature of SMGs toward higher redshifts (as suggested by recent theoretical works; e.g., Behrens et al. 2018; Liang et al. 2019; Ma et al. 2019; Sommovigo et al. 2020; though we note that such evolution is not seen when comparing similar luminosity samples; e.g., Dudzevičiūtė et al. 2020), then the degeneracy between redshift and dust temperature could result in a nonevolving $S_\nu[870\,\mu m]/S_\nu[2\,mm]$ ratio.

To test the ability with which our sample can constrain the evolution of this ratio, we draw on ~2000 simulated sources extracted from output photometry of the Casey et al. (2018b) Model B. This model produces a "dust-rich early universe," where dusty star-forming galaxies dominate the cosmic star formation history at $1.5 \lesssim z \lesssim 6.5$; however, we note that the luminosity function model does not affect the redshift dependence of (sub)millimeter colors. An implicit assumption of this model is that there is no redshift evolution in T_{dust}, although there is a nonevolving luminosity dependence of infrared luminosity with some intrinsic scatter. The emissivity spectral index is assumed to be fixed at $\beta = 1.8$. In other words, redshift evolution of $S_\nu[870\,\mu m]/S_\nu[2\,mm]$ is a fundamental assumption of the model, with scatter caused by variation in dust temperature and observational noise. Simulated sources take into account the effect of the CMB as described in da Cunha et al. (2013) and have analogous flux densities and detection S/Ns to the ALESS sample at 870 μm.

We downsample the ~2000 simulated sources to the sample size and redshift distribution of the ALESS sources in Monte Carlo trials. Within the redshift range of the majority of the ALESS data ($1.2 < z < 5.0$), the redshift evolution of the millimeter color should be linear in $\log(1 + z)$ versus $S_\nu[870\,\mu m]/S_\nu[2\,mm]$. Thus, we fit linear relationships, weighted by S/N in $S_\nu[870\,\mu m]/S_\nu[2\,mm]$, between these quantities for both our simulated Monte Carlo samples from the Casey et al. (2018b) model and the ALESS data, bootstrapping the latter to constrain the uncertainty in the inferred relationship. We show the results in Figure 14, where the measured slope of the relation deviates from the median relation of the model Monte Carlo trials at the 3.3σ level (inset histogram showing bootstrapped slope measured for ALESS sample vs. slope of simulated sources). The flatter measured slope in ALESS hints at a possible breakdown in the assumptions of the model, i.e., that there may be real evolution in dust temperatures and/or β from $1 \lesssim z \lesssim 5$. This is consistent with
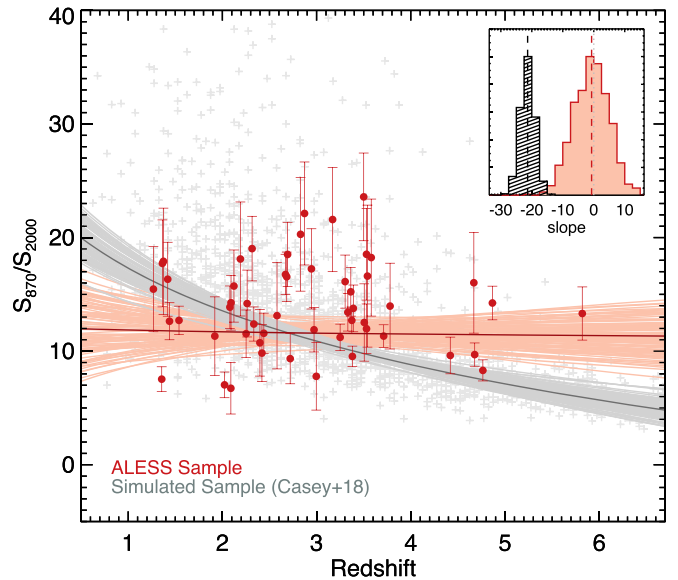

Figure 14. A comparison of the measured slope in $\log(1 + z)$ vs. $S_\nu[870\,\mu m]/S_\nu[2\,mm]$ between the ALESS sample (we include only sources with S/N ⩾ 4 here) and simulated sources from Casey et al. (2018b) as projected in z vs. $S_\nu[870\,\mu m]/S_\nu[2\,mm]$. The light-gray points show the distribution of extracted flux ratios for simulated sources after accounting for the statistical noise of observations of the ALESS sample at both 870 μm and 2 mm. The gray lines represent best fits to Monte Carlo draws from the simulated sources, chosen to have similar S/N and redshift distribution to the ALESS data. The best-fit line to ALESS data is shown in dark red, with orange lines representing the fits to bootstrapped subsamples of ALESS. The inset shows the distribution of best-fit slopes to the simulated data (black) in relation to the measured slope (orange, with bootstrapped uncertainties); the deviation between the two is significant at the ~3.3σ level.

the fact that we find a correlation between T_{dust} and redshift for our well-sampled subset ($r_S = 0.51$, 2.6σ), though that correlation is likely to be due, at least in part, to selection effects (see also Dudzevičiūtė et al. 2020). We find no correlation between β and redshift for the well-sampled subset ($r_S = -0.13$, $< 1\sigma$).

What is clear from this test is that the statistical significance with which the relationship between redshift and $S_\nu[870\,\mu m]/S_\nu[2\,mm]$ is flatter than expected is low, due in part to our relatively small sample size and low S/N on individual sources. A robust characterization of the evolution of this ratio and its implications on measured dust temperatures and emissivity indexes will require samples ~5× larger than currently exist.

5.3. Comparison with Other Measurements and Theoretical Predictions

In Figure 15, we compare our derived dust temperatures and emissivity indexes with those obtained for other samples of galaxies, mostly in the local universe, where such measurements have been possible with Herschel, SCUBA, and Planck. The exact values of these parameters, especially of the dust temperatures, might not be directly comparable between samples, as they can depend strongly on the SED fitting method and wavelength coverage of the data. However, some general conclusions may be derived from this comparison. Both local ultraluminous infrared galaxies (ULIRGs) and high-redshift SMGs show on average warmer dust temperatures, presumably because of their intense star formation activities that produce stronger interstellar radiation fields heating the dust grains. Both moderately star-forming local galaxies from the Herschel Reference sample (Cortese et al. 2014) and the
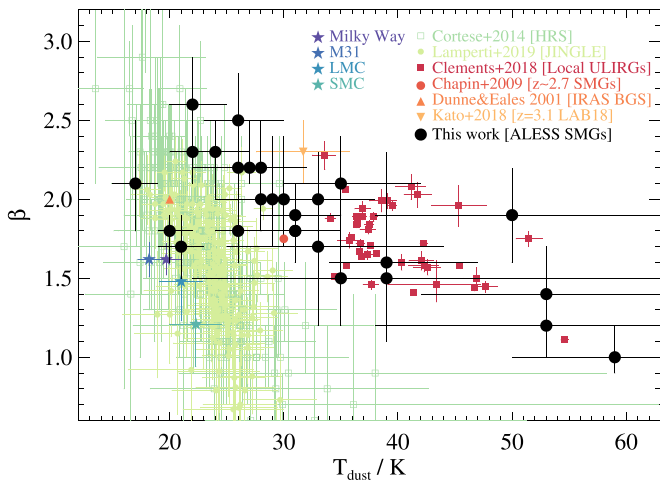
Figure 15. Dust temperature against dust emissivity index for our SMGs and other samples in the literature: local star-forming galaxies from the Herschel Reference Sample (HRS; Cortese et al. 2014) and the JCMT dust and gas In Nearby Galaxies Legacy Exploration (JINGLE) sample (Lamperti et al. 2019), and local ULIRGs from the Herschel ULIRG Survey (HERUS; Clements et al. 2018). The remaining symbols show either single-source measurements (e.g., a $z = 3.1$ Lyα blob from Kato et al. 2018) or average values for galaxy samples (average value for a sample of five SMGs at $z \sim 2.7$ observed with AzTEC at 1.1mm from Chapin et al. 2009; average value for a sample of 32 local infrared galaxies from the IRAS Bright Galaxy Sample observed with SCUBA in the submillimeter by Dunne & Eales 2001). The stars show measurements from Planck for the Milky Way (Planck Collaboration et al. 2014), M31 (Planck Collaboration et al. 2015), and the Magellanic Clouds (Planck Collaboration et al. 2011).

JCMT dust and gas In Nearby Galaxies Legacy Exploration (JINGLE) sample (Lamperti et al. 2019), as well as local ULIRGs from the HERUS sample (Clements et al. 2018), show a negative correlation between T_{dust} and β, and the slope of this correlation is similar to ours in the case of the HERUS sample, though we note that our ALESS SMGs extend to lower temperatures than local ULIRGs (a well-known difference between local ULIRGs and high-redshift SMGs; e.g., Symeonidis et al. 2013; Swinbank et al. 2014). More importantly, our SMGs seem to span a similar range in dust emissivity index to those local samples, with values ranging between $\beta \simeq 1.0$ and 2.5.

Our results are broadly consistent with the best previous constraints of the dust emissivity index in $z \sim 2.7$ SMGs using AzTEC 1.1mm data, which yielded an average value of $\beta \simeq 1.75^{+0.25}_{-0.75}$ for a sample of five SMGs (Chapin et al. 2009). Magnelli et al. (2012) also found on average $\beta = 2.0 \pm 0.2$ for a sample of 19 SMGs observed with all Herschel/PACS and SPIRE bands, plus at least one detection longward of 1 mm, from modeling their SEDs with more complex, multitemperature models. Their quoted error on β is smaller than ours, likely due to better sampling of the SEDs. With our sample we not only confirm this value to be a reasonable average value for high-redshift dusty star-forming galaxies ($\beta \simeq 1.5$–2 is often assumed when modeling sources at both low and high redshift; e.g., Scoville et al. 2016; Galliano et al. 2018) but also show that there can be significant variation from galaxy to galaxy. We note that the recent ALMA measurement of $\beta = 2.3$ in a $z = 3.1$ galaxy by Kato et al. (2018) is entirely consistent with the range of values we find for our SMGs, and therefore that source is not necessarily an outlier in dust properties. The recent sample of 47 SMGs from Birkin et al. (2021) yields $\beta = 2.1 \pm 0.1$, consistent with our results (J. Birkin, private communication).

Aravena et al. (2016) derive $\beta = 1.3 \pm 0.2$ (using the RJ approximation) for a source individually detected at 1.3 and 3 mm in the ASPECS ALMA spectroscopic deep field pilot (Walter et al. 2016), and even lower values ($\beta = 0.9 \pm 0.4$) for a stacked sample. Taken at face value, these results interestingly could indicate different dust emissivity indexes (and therefore different dust-grain properties) in samples of galaxies of lower infrared luminosity than SMGs that are also selected at different wavelengths. However, in Appendix B we demonstrate that the RJ approximation is invalid even for the $\lambda > 1$ mm ASPECS bands at $z > 1$, and that could lead to the emissivity index being underestimated by between 0.2 and 1.0, depending on the exact redshifts and dust temperatures of the sources (Figure 17).

The average dust emissivity index of our SMGs, $\beta = 1.9 \pm 0.4$, is entirely consistent with the predictions of theoretical dust models of interstellar dust (e.g., Draine & Lee 1984; Draine 2011; Köhler et al. 2015), which predict values typically between 1 and 2.5, depending on grain composition. For example, Köhler et al. (2015) predict $\beta \sim 1.5$ for core mantle grains in the diffuse ISM and an increase to $\beta \sim 1.8$–2.0 toward denser environments due to coagulation and accretion onto the dust grains, which change their optical properties (see also, e.g., Jones et al. 2017).

The variation in β is connected with a variation in temperature given the strong correlation between these two properties. A negative correlation between β and T_{dust} not only is found from global SED fits of galaxies but also is well known from fits to the dust emission of galactic molecular clouds and cold cores (e.g., Dupac et al. 2003; Désert et al. 2008; Paradis et al. 2010; Juvela et al. 2013). The existence of this correlation is robust against uncertainties introduced by SED fitting methods, wavelength coverage of the data, etc., and is thought to be a result of a change in the intrinsic emissivity properties of dust grains with temperature. Indeed, laboratory measurements of interstellar dust-grain analogs such as amorphous silicate grains also show a negative correlation between β and temperature (Agladze et al. 1996; Mennella et al. 1998; Boudet et al. 2005; Meny et al. 2007; Coupeaud et al. 2011; see also Appendix B of Inoue et al. 2020). Additional radiative transfer effects could also contribute to this correlation by introducing departures to the isothermal approximation, in the sense that a mix of dust temperatures along the line of sight can contribute to broadening the SEDs and hence lowering the inferred β values (e.g., Shetty et al. 2009; Coupeaud et al. 2011; Köhler et al. 2015).

We conclude that while it is challenging to connect our measured emissivity indexes directly to evolutionary grain models, the typical values found for our SMGs are broadly consistent with local measurements, theoretical dust models, and laboratory measurements. Therefore, there does not seem to be a strong evolution of the dust properties in dusty star-forming galaxies between $z \sim 2.7$ and $z \sim 0$, at least for massive, chemically evolved galaxies such as SMGs.

6. Summary and Conclusions

In this paper we present new ALMA 2 mm continuum observations of the 99 870 μm selected SMGs in the ALESS sample. We find that at the sensitivity of our observations (53 μJy beam^{-1} on average), we detect 70 sources (i.e., 71% of our sample), including 53 above 4σ. We model the dust emission in the ALESS SMGs using isothermal, optically thin models of varying dust temperatures and emissivity indexes, and we also explore more general opacity models where we vary the

wavelength at which the dust becomes optically thin. In order to break degeneracies in the models, we include Herschel fluxes sampling near the peak of the dust emission. This allows us to derive robust dust properties for a subset of 27 ALESS SMGs with well-sampled SEDs and spectroscopic redshifts. The main conclusions of our work are the following:

1. At the depth of our observations, the detection rate of our SMGs at 2 mm is practically independent of redshift, and brighter SMGs (with higher $870\,\mu m$ fluxes and stellar masses) are the most likely to be detected. A total of 29 of the ALESS sources remain undetected in our 2 mm observations; this could be due in part to the depth of our observations, or they may have peculiar dust emission properties.

2. For the sources for which we measure a 2 mm flux density (i.e., $S/N > 1.5$), the median $870\,\mu m$-to-2 mm flux ratio is 14 ± 5. The median flux ratio for the entire ALESS sample, including upper 2 mm upper limits, is 17 ± 9. For our detected sources, we find that this flux ratio does not depend on redshift, which could point to an evolution of dust temperatures and/or emissivity indexes with redshift. This needs to be further explored with larger samples.

3. We demonstrate that the $870\,\mu m$-to-2 mm flux ratio alone cannot be used to derive the emissivity index of the dust β using the RJ approximation. This approximation can lead to a severe underestimation of the true value of β.

4. For a subset of 27 SMGs for which we have well-sampled SEDs and spectroscopic redshifts, we estimate β, T_{dust}, L_{dust}, and M_{dust} using isothermal, optically thin dust models. Including 2 mm observations allows us to constrain β very precisely, to within ± 0.25 for each source, which leads to M_{dust} being constrained to ± 0.08 dex, a twofold improvement in precision when compared to not including 2 mm fluxes in the fitting (in which case β remains unconstrained). The median dust mass of our well-sampled SMGs is $M_{dust} = 5.8^{+5.9}_{-2.4} \times 10^8\,M_\odot$, consistent with previous estimates using MAGPHYS that also assume optically thin dust and $\beta = 1.5$–2 (though multiple temperature components) and no fluxes beyond $870\,\mu m$ (da Cunha et al. 2015). We note, however, that this value and the quoted precision on individual M_{dust} measurements were obtained using the optically thin dust assumption, and additional systematics need to be taken into account, as these values depend strongly on the assumed dust opacity. We find that in our general opacity scenario we would obtain dust masses that are typically three times lower. Our current observations are not sufficient to distinguish between optically thin and optically thick dust. Better sampling of the dust emission near its peak, specifically through high-S/N, high-frequency ALMA observations, could help, as well as more measurements of the dust emission sizes of the sources. Uncertainties in the normalization of the dust emissivity per unit mass can lead to further ~factor of 3 systematic uncertainties in the dust masses (e.g., Galliano et al. 2018; Bianchi et al. 2019; Inoue et al. 2020).

5. We measure a median value of $\beta = 1.9 \pm 0.4$ for the dust emissivity index of our subset of 27 well-sampled SMGs. Contrary to the dust mass estimates, this result is robust against dust opacity assumptions in the models, and it is consistent with previous estimates for local galaxies and with expectations from theoretical modeling and laboratory measurements of interstellar dust-grain analogs.

6. We find a negative correlation between β and T_{dust} that is not introduced by our method but could be introduced, to some extent, by selection effects, since sources with simultaneously high β and high T_{dust} would not be selected in our well-sampled data set. However, this correlation is also found for local galaxy samples and Milky Way dust clouds selected in different ways, and it is predicted by theoretical dust models; therefore, selection effects might not be the only cause for the correlation found in our sample.

This work confirms the dust emissivity index between 1.5 and 2.0 that is typically assumed in most high-redshift studies. This implies that the properties of dust at $z \simeq 1$–3 are similar to the properties of local galaxies. This is true at least for SMGs, which, based on their relatively high stellar masses ($M_* \gtrsim 10^{10}\,M_\odot$; da Cunha et al. 2015; Dudzevičiūtė et al. 2020), are likely to have already reached solar metallicities in their ISM. We speculate that therefore they are likely to have reached a critical metallicity for their dust-grain evolution to be happening mainly through ISM growth (see Dudzevičiūtė et al. 2021), which is also thought to be the dominant mechanism in the Milky Way and other present-day galaxies (e.g., Asano et al. 2013). A larger number of robust measurements of the emissivity index of high-redshift galaxies of lower masses/metallicities with ALMA would help establish whether there is an evolution of the dust-grain properties in galaxies with a less chemically evolved ISM.

Appendix A
Source Positions and ALMA Fluxes

In this appendix, we present the positions and ALMA fluxes of our ALESS sources in Table 1. In Table 2, we list additional 2 mm detected sources that have no counterpart in the main ALESS catalog.

Table 1
Positions and Measured and Deboosted ALMA Fluxes in Band 7 (Hodge et al. 2013) and Band 4 (This Work) of Our 99 ALESS Sources

Source ID	R.A. (J2000)	Decl. (J2000)	$S_\nu^{measured}$[870 μm] (mJy)	$S_\nu^{measured}$[2 mm] (mJy)	S/N[2 mm]	$S_\nu^{deboosted}$[870 μm] (mJy)	$S_\nu^{deboosted}$[2 mm] (mJy)
ALESS001.1	03:33:14.46	−27:56:14.5	6.7 ± 0.5	0.69 ± 0.05	13.8	6.6 ± 0.5	0.68 ± 0.05
ALESS001.2	03:33:14.41	−27:56:11.6	3.5 ± 0.4	0.25 ± 0.05	5.0	3.3 ± 0.4	0.21 ± 0.05
ALESS001.3	03:33:14.18	−27:56:12.3	1.9 ± 0.4	<0.05	<1.5	1.6 ± 0.4	⋯
ALESS002.1	03:33:02.69	−27:56:42.8	3.8 ± 0.4	0.24 ± 0.05	4.8	3.6 ± 0.4	0.20 ± 0.05
ALESS002.2	03:33:03.07	−27:56:42.9	4.2 ± 0.7	0.30 ± 0.05	6.0	3.7 ± 0.7	0.27 ± 0.05
ALESS003.1	03:33:21.50	−27:55:20.3	8.3 ± 0.4	0.66 ± 0.05	13.2	8.2 ± 0.4	0.65 ± 0.05
ALESS005.1	03:31:28.91	−27:59:09.0	7.8 ± 0.7	0.49 ± 0.05	9.8	7.6 ± 0.7	0.47 ± 0.05
ALESS006.1	03:32:56.96	−28:01:00.7	6.0 ± 0.4	0.49 ± 0.05	9.8	5.9 ± 0.4	0.48 ± 0.05
ALESS007.1	03:33:15.42	−27:45:24.3	6.1 ± 0.3	0.35 ± 0.05	7.0	6.1 ± 0.3	0.33 ± 0.05
ALESS009.1	03:32:11.34	−27:52:11.9	8.8 ± 0.5	0.63 ± 0.05	12.6	8.7 ± 0.5	0.61 ± 0.05
ALESS010.1	03:32:19.06	−27:52:14.8	5.2 ± 0.5	0.34 ± 0.05	6.8	5.0 ± 0.5	0.31 ± 0.05
ALESS011.1	03:32:13.85	−27:56:00.3	7.3 ± 0.4	0.46 ± 0.05	9.2	7.2 ± 0.4	0.44 ± 0.05
ALESS013.1	03:32:48.99	−27:42:51.8	8.0 ± 0.6	0.71 ± 0.05	14.2	7.8 ± 0.6	0.70 ± 0.05
ALESS014.1	03:31:52.49	−28:03:19.1	7.5 ± 0.5	0.79 ± 0.05	15.8	7.4 ± 0.5	0.77 ± 0.05
ALESS015.1	03:33:33.37	−27:59:29.6	9.0 ± 0.4	0.55 ± 0.05	11.0	8.9 ± 0.4	0.53 ± 0.05
ALESS015.3	03:33:33.59	−27:59:35.4	2.0 ± 0.5	<0.05	<1.5	1.5 ± 0.5	⋯
ALESS017.1	03:32:07.30	−27:51:20.8	8.4 ± 0.5	0.67 ± 0.05	13.4	8.3 ± 0.5	0.65 ± 0.05
ALESS018.1	03:32:04.88	−27:46:47.7	4.4 ± 0.5	0.39 ± 0.05	7.8	4.2 ± 0.5	0.36 ± 0.05
ALESS019.1	03:32:08.26	−27:58:14.2	5.0 ± 0.4	0.30 ± 0.05	6.0	4.9 ± 0.4	0.26 ± 0.05
ALESS019.2	03:32:07.89	−27:58:24.1	2.0 ± 0.5	0.15 ± 0.05	3.0	1.5 ± 0.5	⋯
ALESS022.1	03:31:46.92	−27:32:39.3	4.5 ± 0.5	0.33 ± 0.05	6.6	4.3 ± 0.5	0.30 ± 0.05
ALESS023.1	03:32:12.01	−28:05:06.5	6.7 ± 0.4	0.51 ± 0.05	10.2	6.6 ± 0.4	0.49 ± 0.05
ALESS023.7	03:32:11.92	−28:05:14.0	1.8 ± 0.5	<0.05	<1.5	1.3 ± 0.5	⋯
ALESS025.1	03:31:56.88	−27:59:39.3	6.2 ± 0.5	0.31 ± 0.05	6.2	6.1 ± 0.4	0.27 ± 0.05
ALESS029.1	03:33:36.90	−27:58:09.3	5.9 ± 0.4	0.48 ± 0.05	9.6	5.8 ± 0.4	0.46 ± 0.05
ALESS031.1	03:31:49.79	−27:57:40.8	8.1 ± 0.4	0.72 ± 0.05	14.4	8.0 ± 0.4	0.71 ± 0.05
ALESS035.1	03:31:10.51	−27:37:15.4	4.4 ± 0.3	0.39 ± 0.05	7.8	4.3 ± 0.3	0.36 ± 0.05
ALESS035.2*	03:31:10.22	−27:37:18.1	1.4 ± 0.4	<0.05	<1.5	1.0 ± 0.4	⋯
ALESS037.1	03:33:36.14	−27:53:50.6	2.9 ± 0.4	0.32 ± 0.05	6.4	2.7 ± 0.4	0.29 ± 0.05
ALESS037.2	03:33:36.36	−27:53:48.3	1.6 ± 0.4	<0.05	<1.5	1.2 ± 0.4	⋯
ALESS039.1	03:31:45.03	−27:34:36.7	4.3 ± 0.3	0.39 ± 0.05	7.8	4.2 ± 0.3	0.36 ± 0.05
ALESS041.1	03:31:10.07	−27:52:36.7	4.9 ± 0.6	0.20 ± 0.05	4.0	4.6 ± 0.6	⋯
ALESS041.3	03:31:10.30	−27:52:40.8	2.7 ± 0.8	0.10 ± 0.05	4.0	1.8 ± 0.8	⋯
ALESS043.1	03:33:06.64	−27:48:02.4	2.3 ± 0.4	0.14 ± 0.05	2.8	2.0 ± 0.4	⋯
ALESS045.1	03:32:25.26	−27:52:30.5	6.0 ± 0.5	0.31 ± 0.05	6.2	5.8 ± 0.5	0.27 ± 0.05
ALESS049.1	03:31:24.72	−27:50:47.1	6.0 ± 0.7	0.36 ± 0.05	7.2	5.7 ± 0.7	0.33 ± 0.05
ALESS049.2	03:31:24.47	−27:50:38.1	1.8 ± 0.5	<0.06	<1.5	1.3 ± 0.5	⋯
ALESS051.1	03:31:45.06	−27:44:27.3	4.7 ± 0.4	0.29 ± 0.05	5.8	4.6 ± 0.4	0.26 ± 0.05
ALESS055.1	03:33:02.22	−27:40:35.5	4.0 ± 0.4	0.53 ± 0.05	10.6	3.8 ± 0.4	0.51 ± 0.05
ALESS055.2*	03:33:02.16	−27:40:41.3	2.4 ± 0.6	<0.05	<1.5	1.8 ± 0.6	⋯
ALESS055.5	03:33:02.35	−27:40:35.4	1.4 ± 0.4	0.10 ± 0.05	2.0	1.0 ± 0.4	⋯
ALESS057.1	03:31:51.92	−27:53:27.1	3.6 ± 0.6	<0.05	<1.5	3.2 ± 0.6	⋯
ALESS059.2	03:33:03.82	−27:44:18.2	1.9 ± 0.4	0.27 ± 0.05	5.4	1.6 ± 0.4	0.23 ± 0.05
ALESS061.1	03:32:45.87	−28:00:23.4	4.3 ± 0.5	0.44 ± 0.05	8.8	4.1 ± 0.4	0.42 ± 0.05
ALESS063.1	03:33:08.45	−28:00:43.8	5.6 ± 0.3	0.42 ± 0.05	8.4	5.5 ± 0.3	0.40 ± 0.05
ALESS065.1	03:32:52.27	−27:35:26.3	4.2 ± 0.4	0.17 ± 0.05	3.4	4.1 ± 0.4	⋯
ALESS066.1	03:33:31.93	−27:54:09.5	2.5 ± 0.5	0.08 ± 0.05	1.6	2.1 ± 0.5	⋯
ALESS067.1	03:32:43.20	−27:55:14.3	4.5 ± 0.4	0.31 ± 0.05	6.2	4.4 ± 0.4	0.28 ± 0.05
ALESS067.2	03:32:43.02	−27:55:14.7	1.7 ± 0.4	<0.05	<1.5	1.3 ± 0.4	⋯
ALESS068.1	03:32:33.33	−27:39:13.6	3.7 ± 0.6	0.30 ± 0.05	6.0	3.3 ± 0.6	0.27 ± 0.05
ALESS069.1	03:31:33.78	−27:59:32.4	4.9 ± 0.6	0.26 ± 0.05	5.2	4.6 ± 0.6	0.23 ± 0.05
ALESS069.2	03:31:34.13	−27:59:28.9	2.4 ± 0.6	0.10 ± 0.05	2.0	1.8 ± 0.6	⋯
ALESS069.3*	03:31:33.97	−27:59:38.3	2.1 ± 0.6	<0.05	<1.5	1.4 ± 0.6	⋯
ALESS070.1	03:31:44.02	−27:38:35.5	5.2 ± 0.4	0.39 ± 0.05	7.8	5.1 ± 0.4	0.36 ± 0.05
ALESS071.1	03:33:05.65	−27:33:28.2	2.9 ± 0.6	0.17 ± 0.05	3.4	2.4 ± 0.6	⋯
ALESS071.3	03:33:06.14	−27:33:23.1	1.4 ± 0.4	<0.05	<1.5	1.0 ± 0.4	⋯
ALESS072.1	03:32:40.40	−27:37:58.1	4.9 ± 0.5	0.38 ± 0.05	7.6	4.7 ± 0.5	0.35 ± 0.05
ALESS073.1	03:32:29.29	−27:56:19.7	6.1 ± 0.5	0.73 ± 0.05	14.6	5.9 ± 0.5	0.72 ± 0.05
ALESS074.1	03:33:09.15	−27:48:17.2	4.6 ± 0.7	0.20 ± 0.05	4.0	4.2 ± 0.7	⋯
ALESS075.1	03:31:27.19	−27:55:51.3	3.2 ± 0.4	0.14 ± 0.05	2.8	3.0 ± 0.4	⋯
ALESS075.4	03:31:26.57	−27:55:55.7	1.3 ± 0.4	<0.06	<1.5	0.8 ± 0.4	⋯
ALESS076.1	03:33:32.34	−27:59:55.6	6.4 ± 0.6	0.57 ± 0.05	11.4	6.2 ± 0.6	0.45 ± 0.05
ALESS079.1	03:32:21.14	−27:56:27.0	4.1 ± 0.4	0.36 ± 0.05	7.2	3.9 ± 0.4	0.33 ± 0.05

Table 1
(Continued)

Source ID	R.A. (J2000)	Decl. (J2000)	$S_\nu^{\mathrm{measured}}$[870 μm] (mJy)	$S_\nu^{\mathrm{measured}}$[2 mm] (mJy)	S/N[2 mm]	$S_\nu^{\mathrm{deboosted}}$[870 μm] (mJy)	$S_\nu^{\mathrm{deboosted}}$[2 mm] (mJy)
ALESS079.2	03:32:21.60	−27:56:24.0	2.0 ± 0.4	<0.06	<1.5	1.7 ± 0.4	⋯
ALESS079.4*	03:32:21.18	−27:56:30.5	1.8 ± 0.5	<0.05	<1.5	1.3 ± 0.5	⋯
ALESS080.1	03:31:42.80	−27:48:36.9	4.0 ± 0.9	0.28 ± 0.05	5.6	3.2 ± 0.9	0.24 ± 0.05
ALESS080.2	03:31:42.62	−27:48:41.0	3.5 ± 0.9	<0.05	<1.5	2.6 ± 0.9	⋯
ALESS082.1	03:32:54.00	−27:38:14.9	1.9 ± 0.5	0.10 ± 0.05	2.0	1.4 ± 0.5	⋯
ALESS083.4	03:33:08.71	−28:05:18.5	1.4 ± 0.4	0.54 ± 0.05	10.8	1.0 ± 0.4	⋯
ALESS084.1	03:31:54.50	−27:51:05.6	3.2 ± 0.6	0.28 ± 0.05	5.6	2.7 ± 0.6	0.24 ± 0.05
ALESS084.2	03:31:53.85	−27:51:04.4	3.2 ± 0.8	<0.06	<1.5	2.4 ± 0.8	⋯
ALESS087.1	03:32:50.88	−27:31:41.5	1.3 ± 0.4	0.17 ± 0.05	3.4	0.8 ± 0.4	⋯
ALESS087.3*	03:32:51.27	−27:31:50.7	2.4 ± 0.6	<0.06	<1.5	1.8 ± 0.6	⋯
ALESS088.1	03:31:54.76	−27:53:41.5	4.6 ± 0.6	0.32 ± 0.05	6.4	4.3 ± 0.6	0.28 ± 0.05
ALESS088.2*	03:31:55.39	−27:53:40.3	2.1 ± 0.5	<0.06	<1.5	1.6 ± 0.5	⋯
ALESS088.5	03:31:55.81	−27:53:47.2	2.9 ± 0.7	<0.08	<1.5	2.2 ± 0.7	⋯
ALESS088.11	03:31:54.95	−27:53:37.6	2.5 ± 0.7	<0.06	<1.5	1.7 ± 0.7	⋯
ALESS092.2	03:31:38.14	−27:43:43.4	2.4 ± 0.7	<0.05	<1.5	1.6 ± 0.7	⋯
ALESS094.1	03:33:07.59	−27:58:05.8	3.2 ± 0.5	0.19 ± 0.05	3.8	2.9 ± 0.5	⋯
ALESS098.1	03:31:29.92	−27:57:22.7	4.8 ± 0.6	0.30 ± 0.06	5.0	4.5 ± 0.6	0.25 ± 0.06
ALESS099.1*	03:32:51.82	−27:55:33.6	2.1 ± 0.4	<0.05	<1.5	1.8 ± 0.4	⋯
ALESS102.1	03:33:35.60	−27:40:23.0	3.1 ± 0.5	0.09 ± 0.05	1.8	2.8 ± 0.5	⋯
ALESS103.3*	03:33:25.04	−27:34:01.1	1.4 ± 0.4	<0.05	<1.5	1.0 ± 0.4	⋯
ALESS107.1	03:31:30.50	−27:51:49.1	1.9 ± 0.4	0.25 ± 0.06	4.2	1.6 ± 0.4	0.20 ± 0.06
ALESS107.3	03:31:30.72	−27:51:55.7	1.5 ± 0.4	0.08 ± 0.06	<1.5	1.1 ± 0.4	⋯
ALESS110.1	03:31:22.66	−27:54:17.2	4.1 ± 0.5	0.26 ± 0.05	5.2	3.9 ± 0.5	0.21 ± 0.05
ALESS110.5	03:31:22.96	−27:54:14.4	2.4 ± 0.6	<0.06	<1.5	1.8 ± 0.6	⋯
ALESS112.1	03:32:48.86	−27:31:13.3	7.6 ± 0.5	0.42 ± 0.05	8.4	7.5 ± 0.5	0.39 ± 0.05
ALESS114.1	03:31:50.49	−27:44:45.3	3.0 ± 0.8	<0.06	<1.5	2.2 ± 0.8	⋯
ALESS114.2	03:31:51.11	−27:44:37.3	2.0 ± 0.5	<0.07	<1.5	1.5 ± 0.5	⋯
ALESS115.1	03:33:49.70	−27:42:34.6	6.9 ± 0.4	0.48 ± 0.06	8.0	6.8 ± 0.4	0.45 ± 0.06
ALESS116.1	03:31:54.32	−27:45:28.9	3.1 ± 0.5	0.22 ± 0.05	4.4	2.8 ± 0.5	0.17 ± 0.05
ALESS116.2	03:31:54.44	−27:45:31.5	3.4 ± 0.6	0.13 ± 0.05	2.6	3.0 ± 0.6	⋯
ALESS118.1	03:31:21.92	−27:49:41.4	3.2 ± 0.5	0.31 ± 0.06	5.2	2.9 ± 0.5	0.27 ± 0.06
ALESS119.1	03:32:56.64	−28:03:25.2	8.3 ± 0.5	0.38 ± 0.05	7.6	8.2 ± 0.5	0.35 ± 0.05
ALESS122.1	03:31:39.54	−27:41:19.7	3.7 ± 0.4	0.53 ± 0.06	8.8	3.5 ± 0.4	0.50 ± 0.06
ALESS124.1	03:32:04.04	−27:36:06.4	3.6 ± 0.6	0.36 ± 0.06	6.0	3.2 ± 0.6	0.32 ± 0.06
ALESS124.4	03:32:03.89	−27:36:00.1	2.2 ± 0.6	<0.06	<1.5	1.6 ± 0.6	⋯
ALESS126.1	03:32:09.61	−27:41:07.7	2.2 ± 0.5	0.1 ± 0.06	1.7	1.7 ± 0.5	⋯

Note. For the 2 mm sources with $1.5 \leqslant \mathrm{S/N} < 4$, we use the measured fluxes; there is no need to correct these for flux boosting because we measure the flux directly at the known position of the 870 μm source.

Table 2
Significant Detections in Our 2 mm Maps That Do Not Have a Counterpart in the ALESS Main Catalog

Field	ID	R.A. (J2000)	Decl. (J2000)	S_ν[870 μm] (mJy)	$S_\nu^{\mathrm{measured}}$[2 mm] (mJy)	S/N[2 mm]	PB[2 mm]	$S_\nu^{\mathrm{deboosted}}$[2 mm] (mJy)	IRAC?[a]
LESS 5	ALESS005_2mm.1	03:31:29.96	−27:58:47.04	PB < 0.2	0.22 ± 0.05	4.4	0.319	0.17 ± 0.05	N
LESS 59	ALESS059_2mm.1	03:33:02.89	−27:44:33.27	PB < 0.2	0.45 ± 0.05	9.0	0.548	0.43 ± 0.05	Y
LESS 59	ALESS059_2mm.2	03:33:03.37	−27:44:26.20	PB < 0.2	0.23 ± 0.05	4.6	0.857	0.19 ± 0.05	N
LESS 76	ALESS076_2mm.1	03:33:34.13	−27:59:48.75	PB < 0.2	0.25 ± 0.05	5.0	0.356	0.21 ± 0.05	N
LESS 83[b]	ALESS083.1	03:33:09.41	−28:05:30.90	1.4 ± 0.4	0.32 ± 0.05	6.4	0.666	0.29 ± 0.05	Y
LESS 92	ALESS092_2mm.1	03:31:37.00	−27:43:41.26	PB < 0.2	0.26 ± 0.05	5.2	0.710	0.21 ± 0.05	Y
LESS 114[c]	ALESS114_2mm.1	03:31:50.30	−27:44:46.84	< 3.9	0.30 ± 0.05	6.0	0.995	0.25 ± 0.05	Y
LESS 114	ALESS114_2mm.2	03:31:48.85	−27:44:29.80	PB < 0.2	0.25 ± 0.06	4.2	0.303	0.20 ± 0.06	N

Notes.
[a] Spitzer/IRAC 3.6 μm counterpart within 1″ in the ECDFS catalog of Damen et al. (2011); 5σ limiting magnitude is $m_{\mathrm{AB}} = 23.8$.
[b] This is one of the supplementary ALESS sources that had been excluded from the main sample for being outside the primary beam of the Band 7 map (Hodge et al. 2013). However, this source does have a measured 870 μm flux in ALESS, and our detection at 2 mm confirms its SMG status. Simpson et al. (2014) estimate a photometric redshift of $z = 2.36^{+0.67}_{-0.22}$ for ALESS083.1 based on SED modeling of its optical/near-IR counterpart, consistent with the average redshift of the ALESS main sample.
[c] This source is spatially offset by ∼3″ from ALESS114.1, and we confirm that it is undetected in the 870 μm observations despite being within the primary beam.

Appendix B
Testing the Rayleigh–Jeans Approximation

In the RJ regime, two flux densities at different frequencies should be perfectly correlated independently of the intrinsic dust temperature and redshift of the source, and indeed the ratio of two (sub)millimeter fluxes is often used to estimate the dust emissivity index (e.g., Aravena et al. 2016). Here we demonstrate that the 870 μm-to-2 mm flux density ratios measured for our sources cannot be used to obtain the dust emissivity index using the RJ approximation.

In the RJ regime, i.e., at sufficiently low frequencies, the Planck function can be approximated as

$$B_\nu(T_{dust}) \approx \frac{2k_B T_{dust}}{c^2}\nu^2, \tag{B1}$$

where k_B is the Boltzmann constant and c is the speed of light. If we combine Equations (4), (3), and (B1) to obtain the dust emission in the RJ regime, the ratio of any two flux densities depends only on the ratio of their frequencies and on the RJ dust emissivity index β_{RJ}:

$$S_{\nu_1} = S_{\nu_2}\left(\frac{\nu_1}{\nu_2}\right)^{2+\beta_{RJ}}. \tag{B2}$$

In Figure 2(b), we use Equation (B2) with $\nu_1 = 345$ GHz (the frequency of our Band 7 observations) and $\nu_2 = 145$ GHz (the frequency of our Band 4 observations) to plot the predicted relation between the 870 μm and 2 mm flux densities in the RJ approximation assuming different values for β_{RJ}. Our observed correlation between the fluxes has a similar slope and seems to be consistent with $\beta_{RJ} \simeq 1$. The dispersion could be explained using different values of β_{RJ} and could go as low as $\beta_{RJ} = 0.5$, as shown in the figure. At face value, it seems that the majority of our sources would have dust emissivity index values of less than 1.5, which is very low compared to the typically assumed values between 1.5 and 2.0. This could be either because the ALESS SMGs indeed have low dust emissivity indexes or because the RJ approximation is not appropriate at our observed frequencies (for the redshifts and dust temperatures of our sample).

To test this, we generate both optically thin and general opacity (with $\lambda_{thick} = 100$ μm, for reference) dust emission models (Section 4.1) with fixed $\beta = 2$ and T_{dust} between 15 and 80 K. Then, we place each model at different redshifts ($z = 0$–10) and compute the ratio of their flux densities $S_\nu[870 \mu m]/S_\nu[2$ mm] at each redshift. In Figure 16, we show how this ratio deviates from the ratio computed assuming the RJ approximation (Equation (B2)) as a function of the model temperature T_{dust} and observed redshift. Not surprisingly, the deviation from RJ increases with redshift, and at fixed redshift it is larger for lower dust temperatures, because both higher redshift and cooler dust temperatures will shift the peak of the dust emission closer to the observed frequencies. The flux ratio overestimation in the RJ approximation leads directly to a systematic underestimation of β in both dust modeling cases. Figure 16(a) shows that even at $z = 0$, Bands 7 and 4 sample the RJ regime (i.e., the deviation is close to zero) only for hot temperatures. At the typical redshift of our SMG sample ($z \simeq 2.7$), the RJ approximation overpredicts the flux ratios by at least 0.15 dex, which translates to an underestimation of the emissivity index by at least $\Delta\beta = 0.5$ (but the difference can be much larger for the cooler dust temperatures). The effect is similar but slightly more pronounced in the general opacity case.

We conclude that the RJ approximation cannot be used to constrain the dust emissivity indexes of our galaxies using our ALMA observations at 870 μm and 2 mm. We also note that caution must be taken when adopting the RJ approximation to derive the dust emissivity index of high-redshift galaxies observed even at lower frequencies with ALMA. We demonstrate this by repeating the test above using the two frequencies used in the ASPECS survey (Aravena et al. 2016; Walter et al. 2016; González-López et al. 2019): 100 GHz (3 mm) and 230 GHz (1.3 mm). As expected, the deviation from the RJ regime is less significant in this case. However, adopting the RJ approximation can still lead to underestimating β by at least $\Delta\beta = 0.5$ at $z \simeq 2.7$ for both the optically thin and general opacity scenarios (see Figure 17).
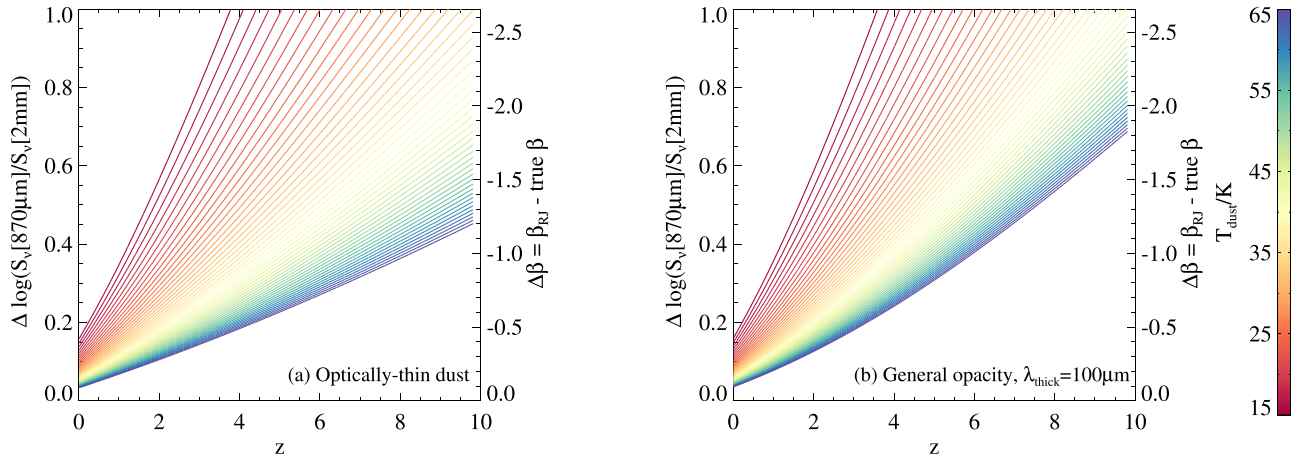

Figure 16. Deviation from the RJ approximation as a function of redshift and temperature. The y-axis shows the difference between the ratio of Band 7 to Band 4 flux densities computed using the RJ approximation (Equation (B2)) and the true ratio, i.e., $\Delta \log(S_\nu[870 \mu m]/S_\nu[2$ mm]) = $\log(S_\nu[870 \mu m]/S_\nu[2$ mm])$_{RJ}$ − $\log(S_\nu[870 \mu m]/S_\nu[2$ mm])$_{true}$, computed using (a) the optically thin approximation (Section 4.1.1) and (b) the general opacity model, where we fix $\lambda_{thick} = 100$ μm (Section 4.1.2). This translates linearly to a difference $\Delta\beta$ between the inferred RJ emissivity index β_{RJ} and the true emissivity index (right-hand y-axes).
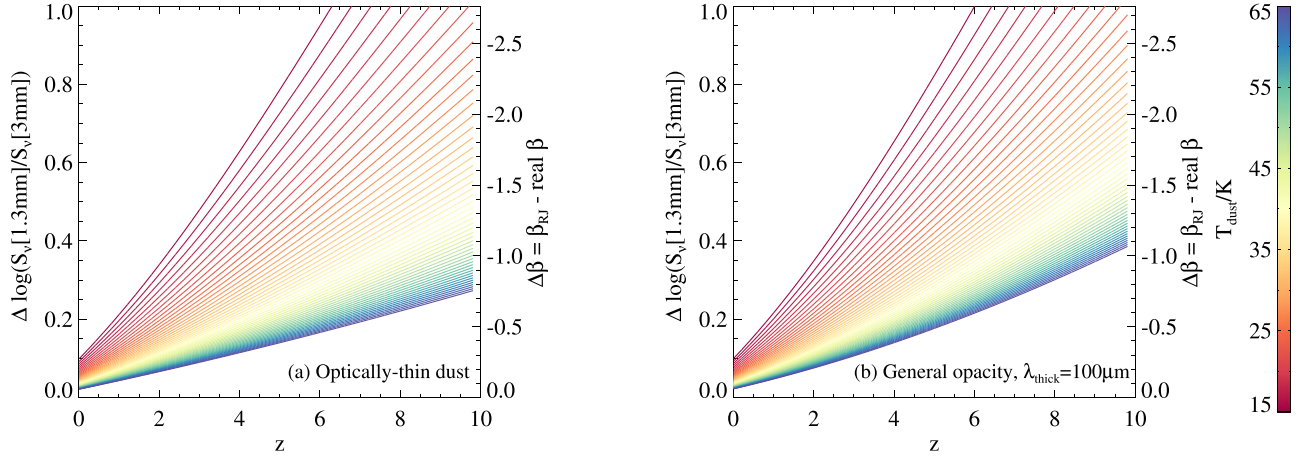
Figure 17. Same as Figure 16, but using the ALMA Band 6 and Band 3 fluxes (at 1.3 mm and 3 mm).

Table 3
Dust Physical Properties of the 27 Galaxies in Our Well-sampled Subset
Derived Using the Optically Thin Dust Approximation (Section 4.1.1)

Source	$T_{\mathrm{dust}}/\mathrm{K}$	β	$\log(L_{\mathrm{dust}}/L_\odot)$	$\log(M_{\mathrm{dust}}/M_\odot)$
ALESS002.1	26^{+4}_{-3}	$2.2^{+0.4}_{-0.4}$	$12.29^{+0.06}_{-0.06}$	$8.70^{+0.08}_{-0.09}$
ALESS003.1	31^{+4}_{-3}	$1.9^{+0.2}_{-0.2}$	$12.76^{+0.09}_{-0.09}$	$8.99^{+0.05}_{-0.06}$
ALESS005.1	28^{+5}_{-3}	$2.2^{+0.3}_{-0.3}$	$12.70^{+0.09}_{-0.09}$	$8.84^{+0.06}_{-0.06}$
ALESS006.1	26^{+3}_{-2}	$1.8^{+0.2}_{-0.2}$	$12.35^{+0.05}_{-0.05}$	$9.10^{+0.04}_{-0.04}$
ALESS007.1	35^{+7}_{-5}	$2.1^{+0.3}_{-0.2}$	$12.96^{+0.15}_{-0.12}$	$8.63^{+0.06}_{-0.06}$
ALESS009.1	50^{+16}_{-12}	$1.9^{+0.3}_{-0.3}$	$13.39^{+0.31}_{-0.28}$	$8.46^{+0.12}_{-0.11}$
ALESS011.1	24^{+3}_{-2}	$2.3^{+0.2}_{-0.3}$	$12.49^{+0.08}_{-0.09}$	$9.00^{+0.08}_{-0.06}$
ALESS017.1	21^{+2}_{-1}	$1.8^{+0.1}_{-0.2}$	$12.10^{+0.04}_{-0.06}$	$9.46^{+0.05}_{-0.03}$
ALESS018.1	39^{+8}_{-5}	$1.6^{+0.3}_{-0.2}$	$12.80^{+0.09}_{-0.08}$	$8.71^{+0.06}_{-0.07}$
ALESS022.1	29^{+5}_{-3}	$2.0^{+0.4}_{-0.3}$	$12.52^{+0.06}_{-0.06}$	$8.76^{+0.07}_{-0.07}$
ALESS023.1	28^{+4}_{-3}	$2.0^{+0.3}_{-0.3}$	$12.54^{+0.11}_{-0.10}$	$8.93^{+0.08}_{-0.07}$
ALESS025.1	26^{+4}_{-3}	$2.5^{+0.3}_{-0.3}$	$12.61^{+0.10}_{-0.09}$	$8.68^{+0.09}_{-0.08}$
ALESS029.1	21^{+3}_{-1}	$1.7^{+0.3}_{-0.2}$	$11.97^{+0.05}_{-0.06}$	$9.28^{+0.05}_{-0.04}$
ALESS031.1	32^{+4}_{-4}	$1.8^{+0.2}_{-0.2}$	$12.71^{+0.08}_{-0.10}$	$9.02^{+0.06}_{-0.06}$
ALESS035.1	53^{+15}_{-11}	$1.4^{+0.3}_{-0.2}$	$13.08^{+0.22}_{-0.21}$	$8.51^{+0.10}_{-0.08}$
ALESS049.1	27^{+5}_{-3}	$2.2^{+0.3}_{-0.1}$	$12.49^{+0.13}_{-0.13}$	$8.71^{+0.10}_{-0.10}$
ALESS061.1	39^{+24}_{-17}	$1.5^{+0.8}_{-0.4}$	$12.57^{+0.52}_{-0.46}$	$8.66^{+0.30}_{-0.24}$
ALESS067.1	30^{+5}_{-3}	$2.0^{+0.4}_{-0.3}$	$12.57^{+0.07}_{-0.06}$	$8.73^{+0.06}_{-0.06}$
ALESS068.1	33^{+12}_{-7}	$1.7^{+0.6}_{-0.5}$	$12.33^{+0.16}_{-0.15}$	$8.59^{+0.12}_{-0.14}$
ALESS070.1	31^{+4}_{-3}	$1.8^{+0.3}_{-0.2}$	$12.56^{+0.06}_{-0.07}$	$8.87^{+0.05}_{-0.05}$
ALESS088.1	17^{+3}_{-2}	$2.1^{+0.4}_{-0.3}$	$11.67^{+0.05}_{-0.04}$	$9.21^{+0.07}_{-0.09}$
ALESS098.1	22^{+3}_{-2}	$2.6^{+0.3}_{-0.3}$	$12.39^{+0.06}_{-0.05}$	$8.91^{+0.05}_{-0.05}$
ALESS107.1	53^{+16}_{-15}	$1.2^{+0.5}_{-0.3}$	$12.54^{+0.28}_{-0.29}$	$8.20^{+0.19}_{-0.15}$
ALESS112.1	22^{+2}_{-2}	$2.3^{+0.3}_{-0.2}$	$12.38^{+0.04}_{-0.06}$	$9.10^{+0.05}_{-0.05}$
ALESS115.1	33^{+5}_{-4}	$2.0^{+0.3}_{-0.2}$	$12.82^{+0.11}_{-0.10}$	$8.74^{+0.07}_{-0.07}$
ALESS118.1	35^{+8}_{-6}	$1.5^{+0.4}_{-0.3}$	$12.35^{+0.09}_{-0.07}$	$8.66^{+0.09}_{-0.09}$
ALESS122.1	59^{+9}_{-9}	$1.0^{+0.2}_{-0.1}$	$12.99^{+0.14}_{-0.12}$	$8.66^{+0.08}_{-0.08}$

Note. For each property, we indicate our best estimate and confidence range, given by the median and 16th–84th percentile range of the posterior likelihood distribution, respectively.

Appendix C
Dust Parameters Derived for Our Well-sampled Subset

In Table 3, we list the median likelihood estimates of the dust physical properties of our 27 sources with well-sampled SEDs and spectroscopic redshifts (and their respective confidence ranges) obtained using the isothermal, optically thin dust assumption.

Appendix D
Further Tests of the Accuracy of Our Fitting Method

D.1. Effect of Unavailable Band 4 or Herschel Data

Here we use mock dust SED fits similar to the ones presented in Section 4.3 to test the effect of excluding fluxes in certain bands from our fits. Figures 18 and 19 show cases where the SED is not as well sampled as in the simulation shown in Figure 12, i.e., excluding the 2 mm data and the Herschel data, respectively. Figure 18 shows that not extending the observations into wavelengths longer than 870 μm impacts the estimates of β significantly; however, the accuracy of the remaining parameters is not significantly affected. That is, if no observations sampling the RJ tail of the dust emission (e.g., at 2 mm) are available, we can still recover the temperature, and consequently the total luminosity and dust mass, albeit with lower average accuracy. On the other hand, if the peak of the SED is not well sampled, as shown in Figure 19, where only the 870 μm and 2 mm fluxes are included in the fits, L_{dust} and T_{dust} become very hard to constrain and inaccurate. Surprisingly, the dust masses are still reasonably accurate (within about 0.5 dex) even in this case. We attribute this to the fact that the parameter priors are realistic (at least in the simulation, since the mock SED parameters are drawn from the sample distribution as the priors used in the fitting). When applying this to real galaxies, the effects of lacking data could be much worse if the real distribution of parameters differs significantly from the priors.

D.2. Effect of Using Optically Thin Models to Fit General Opacity Dust

Here we test the effect of using the wrong assumption regarding dust optical depth on the accuracy of our results. We generate a suite of dust emission models using our general opacity scenario (Section 4.1.2), with a uniform prior on λ_{thick} varying between 60 and 140 μm. Then, we use our Bayesian fitting routine to fit the mock SEDs produced by these models, but assuming only optically thin dust. Figure 20 shows the results of that exercise. We find that our constraints on β and L_{dust} are robust against dust optical depth assumptions; however, significant systematics may arise in T_{dust} and, consequently, the inferred dust masses. These systematics are larger when the input models have higher λ_{thick} (i.e., they deviate more from the optically thin assumption) and hotter dust temperatures, because both of these will affect the peak of the dust emission SED more significantly.
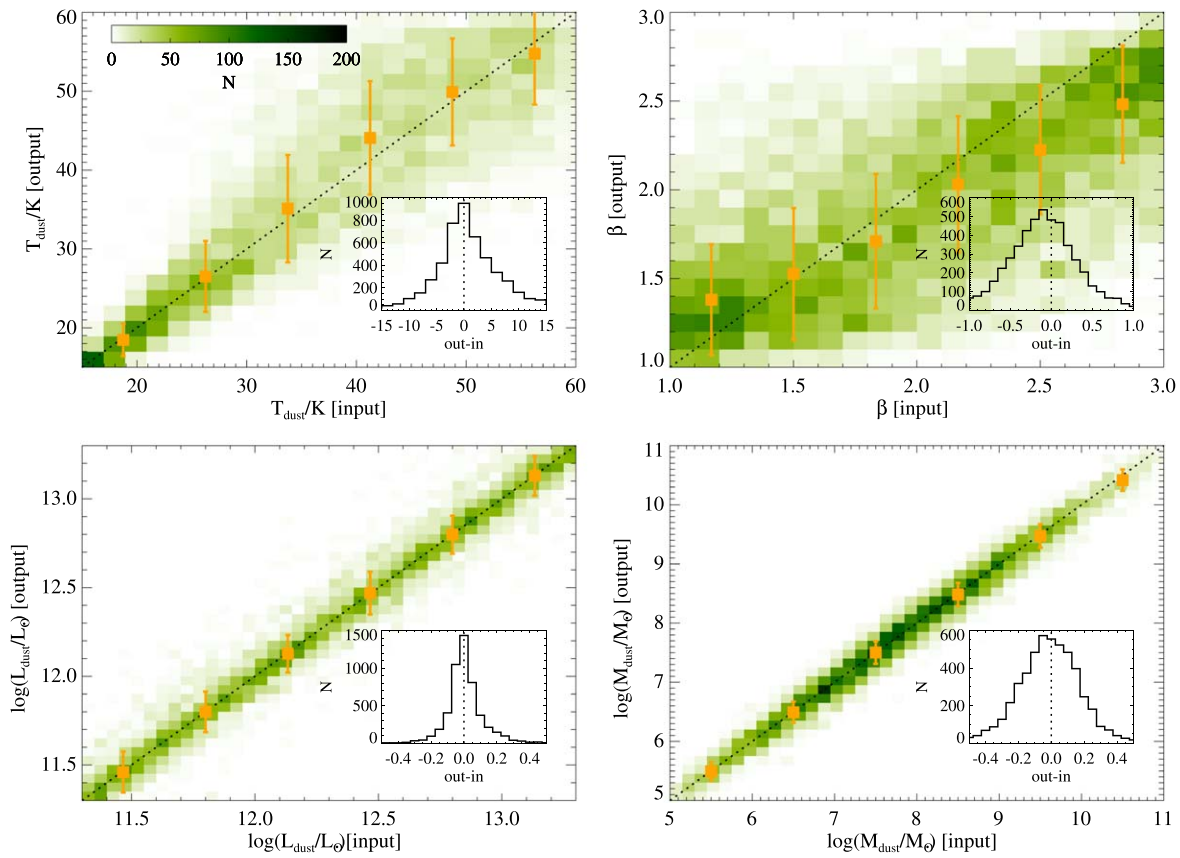
Figure 18. Same as Figure 12, but excluding Band 4 from the fits. This shows that L_{dust} is still robust without low-frequency data, because the fits include data sampling the peak of the SED. The main effect of not having Band 4 is that the accuracy in β decreases significantly, which affects the accuracy in T_{dust} to some extent (because of the degeneracy between these two parameters) and most importantly affects M_{dust} estimates.
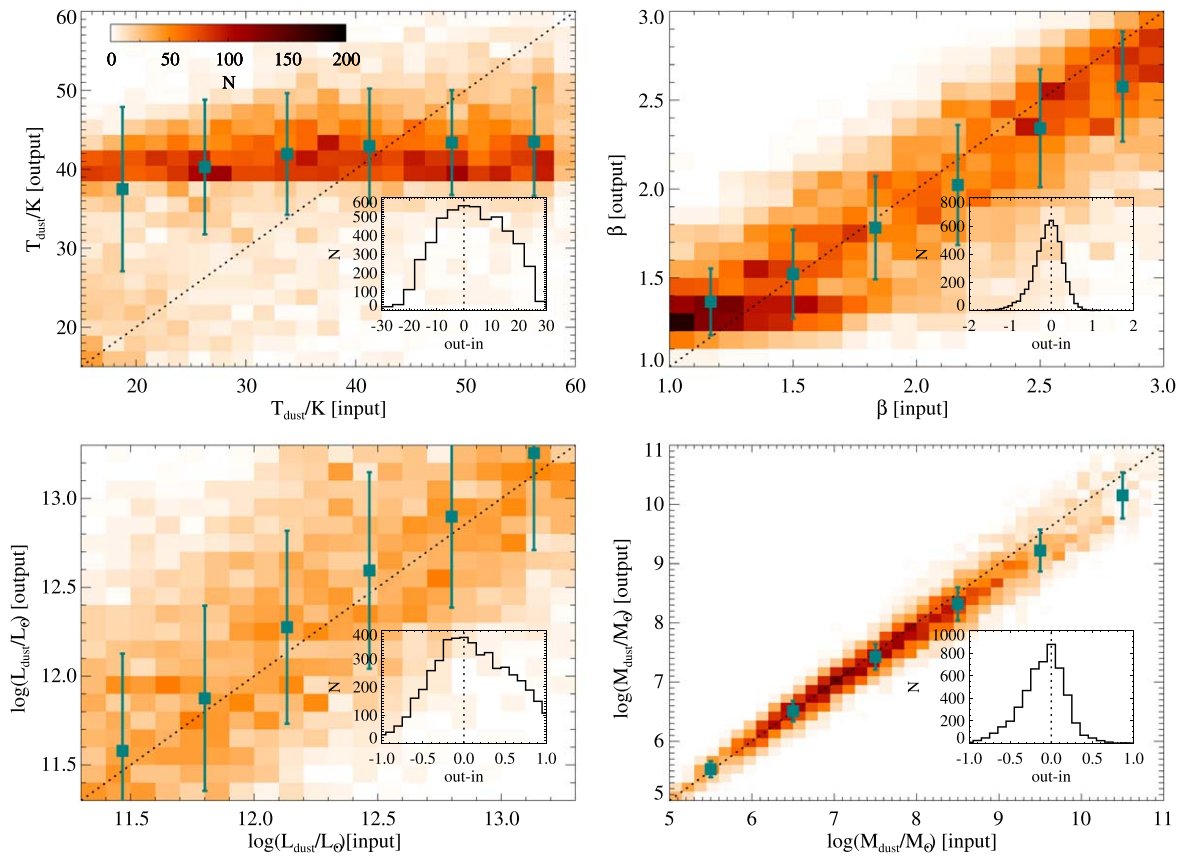
Figure 19. Same as Figure 12, but excluding Herschel data from the fits (i.e., only fitting fluxes in ALMA Bands 7 and 4 here). This shows that we need to sample the peak of the SED to get reliable T_{dust}, and hence also L_{dust} and M_{dust}. β is relatively well constrained, but with larger errors.
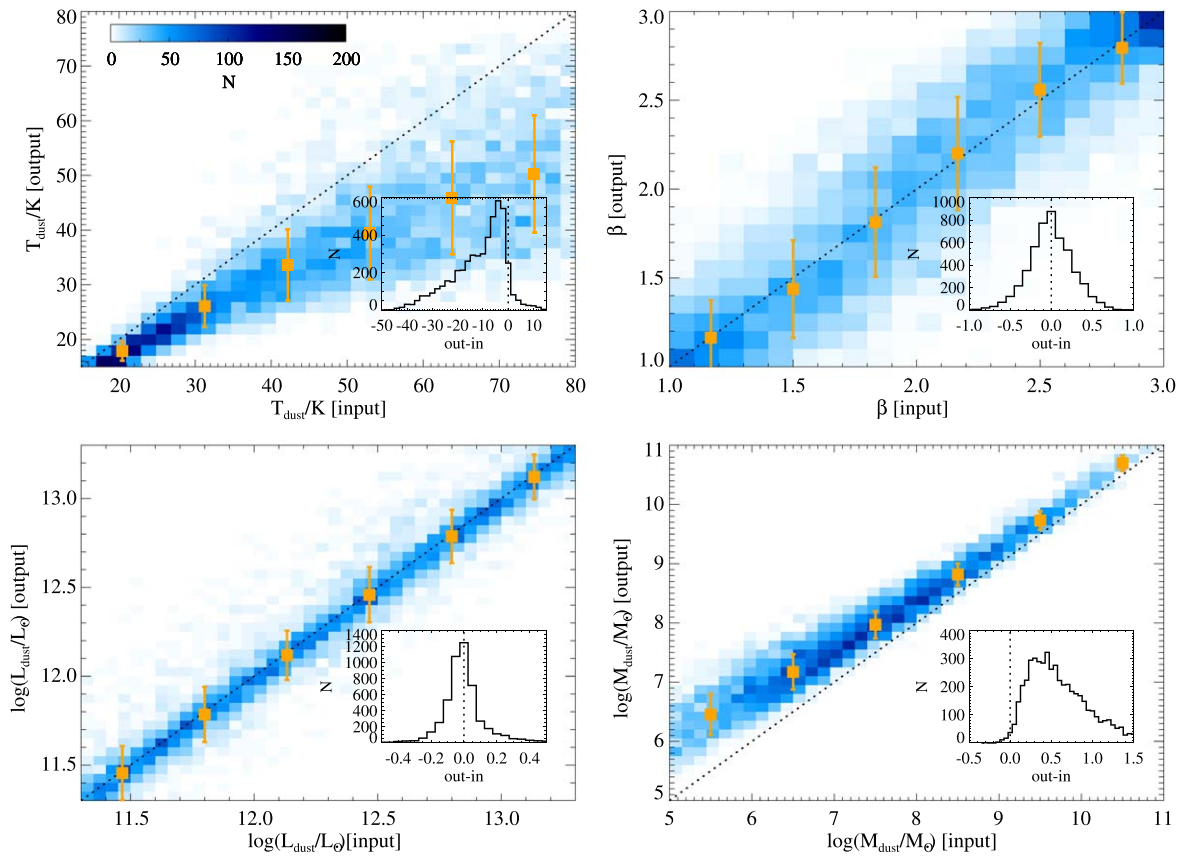
Figure 20. Same as Figure 12, but using general opacity models to generate the mock observations (input) and then fitting those observations with optically thin models (output). This shows that, for the range of general opacity models used (λ_{thick} varying between 60 and 140 μm), the constraints on β and L_{dust} are robust; however, important systematic offsets are seen in T_{dust} and M_{dust}.

ORCID iDs

E. da Cunha https://orcid.org/0000-0001-9759-4797
J. A. Hodge https://orcid.org/0000-0001-6586-8845
C. M. Casey https://orcid.org/0000-0002-0930-6466
H. S. B. Algera https://orcid.org/0000-0002-4205-9567
M. Kaasinen https://orcid.org/0000-0002-1173-2579
I. Smail https://orcid.org/0000-0003-3037-257X
F. Walter https://orcid.org/0000-0003-4793-7880
W. N. Brandt https://orcid.org/0000-0002-0167-2453
H. Dannerbauer https://orcid.org/0000-0001-7147-3575
R. Decarli https://orcid.org/0000-0002-2662-8803
B. A. Groves https://orcid.org/0000-0002-9768-0246
K. K. Knudsen https://orcid.org/0000-0002-7821-8873
A. M. Swinbank https://orcid.org/0000-0003-1192-5837
J. A. Zavala https://orcid.org/0000-0002-7051-1100

References

Agladze, N. I., Sievers, A. J., Jones, S. A., Burlitch, J. M., & Beckwith, S. V. W. 1996, ApJ, 462, 1026
Aravena, M., Decarli, R., Walter, F., et al. 2016, ApJ, 833, 68
Aretxaga, I., Wilson, G. W., Aguilar, E., et al. 2011, MNRAS, 415, 3831
Asano, R. S., Takeuchi, T. T., Hirashita, H., & Inoue, A. K. 2013, EP&S, 65, 213
Barger, A. J., Cowie, L. L., Sanders, D. B., et al. 1998, Natur, 394, 248
Barger, A. J., Wang, W.-H., Cowie, L. L., et al. 2012, ApJ, 761, 89
Behrens, C., Pallottini, A., Ferrara, A., Gallerani, S., & Vallini, L. 2018, MNRAS, 477, 552
Bertoldi, F., Carilli, C., Aravena, M., et al. 2007, ApJS, 172, 132
Bianchi, S. 2013, A&A, 552, A89
Bianchi, S., Casasola, V., Baes, M., et al. 2019, A&A, 631, A102

Birkin, J. E., Weiss, A., Wardlow, J. L., et al. 2021, MNRAS, 501, 3926
Blain, A. W., Smail, I., Ivison, R. J., Kneib, J.-P., & Frayer, D. T. 2002, PhR, 369, 111
Boudet, N., Mutschke, H., Nayral, C., et al. 2005, ApJ, 633, 272
Casey, C. M., Hodge, J., Zavala, J. A., et al. 2018a, ApJ, 862, 78
Casey, C. M., Narayanan, D., & Cooray, A. 2014, PhR, 541, 45
Casey, C. M., Zavala, J. A., Aravena, M., et al. 2019, ApJ, 887, 55
Casey, C. M., Zavala, J. A., Spilker, J., et al. 2018b, ApJ, 862, 77
Chapin, E. L., Pope, A., Scott, D., et al. 2009, MNRAS, 398, 1793
Chapman, S. C., Blain, A. W., Smail, I., & Ivison, R. J. 2005, ApJ, 622, 772
Chen, C.-C., Hodge, J. A., Smail, I., et al. 2017, ApJ, 846, 108
Clements, D. L., Pearson, C., Farrah, D., et al. 2018, MNRAS, 475, 2097
Conley, A., Cooray, A., Vieira, J. D., et al. 2011, ApJL, 732, L35
Cortese, L., Fritz, J., Bianchi, S., et al. 2014, MNRAS, 440, 942
Cortzen, I., Magdis, G. E., Valentino, F., et al. 2020, A&A, 634, L14
Coupeaud, A., Demyk, K., Meny, C., et al. 2011, A&A, 535, A124
da Cunha, E., Charlot, S., & Elbaz, D. 2008, MNRAS, 388, 1595
da Cunha, E., Groves, B., Walter, F., et al. 2013, ApJ, 766, 13
da Cunha, E., Walter, F., Smail, I. R., et al. 2015, ApJ, 806, 110
Damen, M., Labbé, I., van Dokkum, P. G., et al. 2011, ApJ, 727, 1
Danielson, A. L. R., Swinbank, A. M., Smail, I., et al. 2017, ApJ, 840, 78
Davé, R., Oppenheimer, B. D., & Finlator, K. 2011, MNRAS, 415, 11
Désert, F.-X., Macías-Pérez, J. F., Mayet, F., et al. 2008, A&A, 481, 411
Draine, B. T. 2011, Physics of the Interstellar and Intergalactic Medium (Princeton, NJ: Princeton Univ. Press)
Draine, B. T., & Lee, H. M. 1984, ApJ, 285, 89
Draine, B. T., & Li, A. 2007, ApJ, 657, 810
Dudzevičiūtė, U., Smail, I., Swinbank, A. M., et al. 2020, MNRAS, 494, 3828
Dudzevičiūtė, U., Smail, I., Swinbank, A. M., et al. 2021, MNRAS, 500, 942
Dunne, L., & Eales, S. A. 2001, MNRAS, 327, 697
Dupac, X., Bernard, J.-P., Boudet, N., et al. 2003, A&A, 404, L11
Dwek, E., Galliano, F., & Jones, A. P. 2007, ApJ, 662, 927
Eales, S., Bertoldi, F., Ivison, R., et al. 2003, MNRAS, 344, 169
Galliano, F., Galametz, M., & Jones, A. P. 2018, ARA&A, 56, 673
Geach, J. E., Dunlop, J. S., Halpern, M., et al. 2017, MNRAS, 465, 1789
González-López, J., Decarli, R., Pavesi, R., et al. 2019, ApJ, 882, 139

Greve, T. R., Pope, A., Scott, D., et al. 2008, MNRAS, 389, 1489
Groves, B. A., Schinnerer, E., Leroy, A., et al. 2015, ApJ, 799, 96
Gullberg, B., Smail, I., Swinbank, A. M., et al. 2019, MNRAS, 490, 4956
Hayward, C. C., Kereš, D., Jonsson, P., et al. 2011, ApJ, 743, 159
Hodge, J. A., Carilli, C. L., Walter, F., et al. 2012, ApJ, 760, 11
Hodge, J. A., & da Cunha, E. 2020, RSOS, 7, 200556
Hodge, J. A., Karim, A., Smail, I., et al. 2013, ApJ, 768, 91
Hodge, J. A., Riechers, D., Decarli, R., et al. 2015, ApJL, 798, L18
Hodge, J. A., Smail, I., Walter, F., et al. 2019, ApJ, 876, 130
Hodge, J. A., Swinbank, A. M., Simpson, J. M., et al. 2016, ApJ, 833, 103
Högbom, J. A. 1974, A&AS, 15, 417
Hughes, D. H., Serjeant, S., Dunlop, J., et al. 1998, Natur, 394, 241
Inoue, A. K., Hashimoto, T., Chihara, H., & Koike, C. 2020, MNRAS, 495, 1577
Jones, A. P., Köhler, M., Ysard, N., Bocchio, M., & Verstraete, L. 2017, A&A, 602, A46
Juvela, M., Montillaud, J., Ysard, N., & Lunttila, T. 2013, A&A, 556, A63
Juvela, M., & Ysard, N. 2012, A&A, 541, A33
Kaasinen, M., Scoville, N., Walter, F., et al. 2019, ApJ, 880, 15
Karim, A., Swinbank, A. M., Hodge, J. A., et al. 2013, MNRAS, 432, 2
Kato, Y., Matsuda, Y., Iono, D., et al. 2018, PASJ, 70, L6
Kelly, B. C., Shetty, R., Stutz, A. M., et al. 2012, ApJ, 752, 55
Köhler, M., Ysard, N., & Jones, A. P. 2015, A&A, 579, A15
Lamperti, I., Saintonge, A., De Looze, I., et al. 2019, MNRAS, 489, 4389
Liang, L., Feldmann, R., Kereš, D., et al. 2019, MNRAS, 489, 1397
Lianou, S., Barmby, P., Mosenkov, A. A., Lehnert, M., & Karczewski, O. 2019, A&A, 631, A38
Ma, X., Hayward, C. C., Casey, C. M., et al. 2019, MNRAS, 487, 1844
Magnelli, B., Karim, A., Staguhn, J., et al. 2019, ApJ, 877, 45
Magnelli, B., Lutz, D., Santini, P., et al. 2012, A&A, 539, A155
Mancini, M., Schneider, R., Graziani, L., et al. 2015, MNRAS, 451, L70
Mennella, V., Brucato, J. R., Colangeli, L., et al. 1998, ApJ, 496, 1058
Meny, C., Gromov, V., Boudet, N., et al. 2007, A&A, 468, 171
Morgan, H. L., & Edmunds, M. G. 2003, MNRAS, 343, 427
Paradis, D., Veneziani, M., Noriega-Crespo, A., et al. 2010, A&A, 520, L8

Planck Collaboration, Abergel, A., Ade, P. A. R., et al. 2014, A&A, 571, A11
Planck Collaboration, Ade, P. A. R., Aghanim, N., et al. 2011, A&A, 536, A17
Planck Collaboration, Ade, P. A. R., Aghanim, N., et al. 2015, A&A, 582, A28
Planck Collaboration, Aghanim, N., Akrami, Y., et al. 2020, A&A, 641, A6
Riechers, D. A., Bradford, C. M., Clements, D. L., et al. 2013, Natur, 496, 329
Rowlands, K., Dunne, L., Dye, S., et al. 2014, MNRAS, 441, 1017
Rybak, M., Calistro Rivera, G., Hodge, J. A., et al. 2019, ApJ, 876, 112
Sargent, M. T., Béthermin, M., Daddi, E., & Elbaz, D. 2012, ApJL, 747, L31
Scoville, N., Aussel, H., Sheth, K., et al. 2014, ApJ, 783, 84
Scoville, N., Lee, N., Vanden Bout, P., et al. 2017, ApJ, 837, 150
Scoville, N., Sheth, K., Aussel, H., et al. 2016, ApJ, 820, 83
Shetty, R., Kauffmann, J., Schnee, S., Goodman, A. A., & Ercolano, B. 2009, ApJ, 696, 2234
Simpson, J. M., Smail, I., Dudzevičiūtė, U., et al. 2020, MNRAS, 495, 3409
Simpson, J. M., Smail, I., Swinbank, A. M., et al. 2015, ApJ, 799, 81
Simpson, J. M., Smail, I., Swinbank, A. M., et al. 2017, ApJ, 839, 58
Simpson, J. M., Swinbank, A. M., Smail, I., et al. 2014, ApJ, 788, 125
Smail, I., Ivison, R. J., & Blain, A. W. 1997, ApJL, 490, L5
Smolčić, V., Aravena, M., Navarrete, F., et al. 2012, A&A, 548, A4
Sommovigo, L., Ferrara, A., Pallottini, A., et al. 2020, MNRAS, 497, 956
Stach, S. M., Smail, I., Swinbank, A. M., et al. 2018, ApJ, 860, 161
Staguhn, J. G., Kovács, A., Arendt, R. G., et al. 2014, ApJ, 790, 77
Swinbank, A. M., Dye, S., Nightingale, J. W., et al. 2015, ApJL, 806, L17
Swinbank, A. M., Karim, A., Smail, I., et al. 2012, MNRAS, 427, 1066
Swinbank, A. M., Simpson, J. M., Smail, I., et al. 2014, MNRAS, 438, 1267
Symeonidis, M., Vaccari, M., Berta, S., et al. 2013, MNRAS, 431, 2317
Vieira, J. D., Crawford, T. M., Switzer, E. R., et al. 2010, ApJ, 719, 763
Vieira, J. D., Marrone, D. P., Chapman, S. C., et al. 2013, Natur, 495, 344
Walter, F., Decarli, R., Aravena, M., et al. 2016, ApJ, 833, 67
Wang, S. X., Brandt, W. N., Luo, B., et al. 2013, ApJ, 778, 179
Wardlow, J. L., Simpson, J. M., Smail, I., et al. 2018, MNRAS, 479, 3879
Weiß, A., Kovács, A., Coppin, K., et al. 2009, ApJ, 707, 1201
Yun, M. S., Scott, K. S., Guo, Y., et al. 2012, MNRAS, 420, 957
Zavala, J. A., Aretxaga, I., & Hughes, D. H. 2014, MNRAS, 443, 2384
Zavala, J. A., Casey, C. M., Manning, S. M., et al. 2021, ApJ, 909, 165